Naval Research Laboratory

Washington, DC 20375-5000

NRL Memorandum Report 6436

Three Dimensional Equilibrium and Stability of Ionospheric Plasma Clouds

J. F. DRAKE,* M. MULBRANDON AND J. D. HUBA

Geophysical and Plasma Dynamics Branch
Plasma Physics Division

**Science Applications International Corporation*
McLean, VA 22102

March 22, 1989

This research was supported by DNA under Project/Task Code and Title: RB RC/Atmospheric Effects and Mitigation; Work Unit Code and Title: 00166/Plasma Structure Evolution.

SECURITY CLASSIFICATION OF THIS PAGE

REPORT DOCUMENTATION PAGE

Form Approved
OMB No. 0704-0188

1a REPORT SECURITY CLASSIFICATION UNCLASSIFIED	1b RESTRICTIVE MARKINGS
2a SECURITY CLASSIFICATION AUTHORITY	3 DISTRIBUTION/AVAILABILITY OF REPORT Approved for public release; distribution unlimited.
2b DECLASSIFICATION/DOWNGRADING SCHEDULE	
4 PERFORMING ORGANIZATION REPORT NUMBER(S) NRL Memorandum Report 6436	5 MONITORING ORGANIZATION REPORT NUMBER(S)
6a NAME OF PERFORMING ORGANIZATION Naval Research Laboratory 6b OFFICE SYMBOL (If applicable) Code 4780	7a NAME OF MONITORING ORGANIZATION
6c ADDRESS (City, State, and ZIP Code) Washington, DC 20375-5000	7b ADDRESS (City, State, and ZIP Code)
8a NAME OF FUNDING/SPONSORING ORGANIZATION Defense Nuclear Agency 8b OFFICE SYMBOL (If applicable) RAAE	9 PROCUREMENT INSTRUMENT IDENTIFICATION NUMBER
8c ADDRESS (City, State, and ZIP Code) Washington, DC 20305	10 SOURCE OF FUNDING NUMBERS PROGRAM ELEMENT NO: MIPR88-526 / PROJECT NO: RB RC / TASK NO: 00166 / WORK UNIT ACCESSION NO:

11 TITLE (Include Security Classification)
Three Dimensional Equilibrium and Stability of Ionospheric Plasma Clouds

12 PERSONAL AUTHOR(S)
Drake,* J.F., Mulbrandon, M. and Huba, J.D.

13a TYPE OF REPORT	13b TIME COVERED	14 DATE OF REPORT (Year, Month, Day)	15 PAGE COUNT
Interim	FROM _____ TO _____	1989 March 22	70

16 SUPPLEMENTARY NOTATION
(See page ii)

17 COSATI CODES			18 SUBJECT TERMS (Continue on reverse if necessary and identify by block number)
FIELD	GROUP	SUB-GROUP	Barium Clouds Ionospheric Distrubances E x B instability

19 ABSTRACT (Continue on reverse if necessary and identify by block number)

The equilibrium and stability of three dimensional ionospheric plasma clouds is investigated. The equilibrium density profile is assumed to be a 3D waterbag with a circular cross-section transverse to $\underset{\sim}{B}$, and an ellipsoidal cross-section parallel to $\underset{\sim}{B}$. The equilibrium potential consists of two parts: a polarization potential driven by a uniform neutral wind, and an ambipolar potential driven by parallel electron pressure. The latter potential is shown to cause sheared azimuthal plasma flows perpendicular to $\underset{\sim}{B}$. A stability analysis of this equilibrium is carried out. It is found that the $\underset{\sim}{E} \times \underset{\sim}{B}$ instability, which causes the structuring of ionospheric plasma clouds, can be stabilized by the shear in the azimuthal flow. A marginal stability criterion is derived. On the basis of this stability criteria, striations of barium clouds in the ionospheric F region should be stable to further bifurcation, as is observed.

20 DISTRIBUTION/AVAILABILITY OF ABSTRACT	21 ABSTRACT SECURITY CLASSIFICATION
☒ UNCLASSIFIED/UNLIMITED ☐ SAME AS RPT ☐ DTIC USERS	UNCLASSIFIED
22a NAME OF RESPONSIBLE INDIVIDUAL J. D. Huba	22b TELEPHONE (Include Area Code) (202) 767-3630 22c OFFICE SYMBOL Code 4780

DD Form 1473, JUN 86 *Previous editions are obsolete* SECURITY CLASSIFICATION OF THIS PAGE

S/N 0102-LF-014-6603

16. SUPPLEMENTARY NOTATION

*Science Applications International Corporation, McLean, VA 22102.

This research was supported by DNA under Project/Task Code and Title: RB RC/ Atmospheric Effects and Mitigation; Work Unit Code and Title: 00166/Plasma Structure Evolution.

CONTENTS

THREE DIMENSIONAL EQUILIBRIUM AND STABILITY OF IONOSPHERIC PLASMA CLOUDS

I. INTRODUCTION

The dynamic evolution of artificial plasma clouds in the earth's ionosphere has been the subject of scientific study since the early 1960's when the first barium clouds were released. The initial motivation for these experiments was of a diagnostic nature; the motion of the neutral and ionized barium cloud can serve as a means to estimate the magnitude of ambient electric fields and neutral winds in the ionosphere. However, it was soon discovered that ionized barium clouds not only undergo gross translational motions, but also rapidly structure and break into smaller pieces. The instability responsible for this structuring is the $\underset{\sim}{E} \times \underset{\sim}{B}$ instability which was first proposed to explain striations in weakly collisional laboratory plasmas,[1,2] and later applied to barium clouds.[3]

Because of this interesting behavior, a considerable amount of research has been devoted to understanding the dynamics of barium clouds. The types of studies that have been performed concern the linear and nonlinear evolution of the $\underset{\sim}{E} \times \underset{\sim}{B}$ instability,[4-19] as well as large-scale numerical simulations of ionospheric barium clouds.[20-24] In the bulk of these studies, it has been assumed that the ambient magnetic field lines are equipotentials, i.e., the electric field maps perfectly along B, so that only the two dimensional motion of the plasma transverse to B needs to be modelled. For the most part, this is a reasonable assumption since the ratio of the parallel to perpendicular conductivity in the F region of the ionosphere is very large ($\sigma_{\parallel}/\sigma_{\perp} \sim 10^6$). However, in recent studies this assumption has been relaxed and it has been demonstrated that three dimensional effects can have a dramatic impact on the gross stability of ionospheric barium clouds.[16-19]

Manuscript approved July 14, 1988.

A number of theoretical analyses of the influence of three dimensional effects on the evolution of barium clouds have been published,[16-19] and 3D numerical simulation codes have recently been developed.[25,26] In Sperling et al.[16] and Drake et al.[17] the plasma cloud is modelled as a 1D slab transverse to $\underset{\sim}{B}$, and as a 1D waterbag parallel to $\underset{\sim}{B}$ (the cloud had a finite extent along $\underset{\sim}{B}$). In this work the parallel (along $\underset{\sim}{B}$) dynamics coupled the unstable modes to the background plasma outside of the cloud. The distance the unstable modes map into the background plasma is roughly given by $\lambda_{||} \sim \lambda_{\perp} (\sigma_{||}/\sigma_{\perp})^{1/2}$ where $\lambda_{||,\perp}$ denotes the parallel and perpendicular wavelength relative to $\underset{\sim}{B}$, respectively.[27] The coupling to the background plasma was found to be stabilizing, and hence, modes with small transverse wavelengths are more unstable than modes with large transverse wavelengths. The shortcomings of this model[16,17] are that (1) it is restricted to modes with $\lambda_{\perp} << L_n$ where L_n is the density gradient scale length of the plasma cloud transverse to $\underset{\sim}{B}$ (it should be noted that the gross structuring of plasma clouds occurs for $\lambda_{\perp} > L_n$), and (2) it neglects important 2D effects transverse to $\underset{\sim}{B}$ associated with the polarization field of the cloud.

These two shortcomings were redressed in Drake and Huba.[18] In this work a cylindrical 2D waterbag cloud, aligned along the magnetic field, and immersed in a uniform neutral wind is considered. The equilibrium potential produced by the neutral wind was derived, and a 3D stability analysis was performed. An important new physical result was obtained. The combination of finite parallel wavelengths ($k_{||} = 2\pi/\lambda_{||} \neq 0$) and temperature produces an azimuthal drift (V_d) of the plasma perturbations of the cloud. When this azimuthal drift is greater than the drift V_b of the background plasma around the cloud (produced by the equilibrium potential in the cloud frame), the plasma cloud is stable. Physically,

this stabilization criterion ($V_d > V_b$) arises because of the convection of modes from the unstable 'backside' of the cloud to the stable 'frontside'. The major weakness of this calculation is the assumption that the plasma cloud is infinite along $\underset{\sim}{B}$. The 3D effects considered only arise because the perturbations in the stability analysis have finite $k_{||}$. The equilibrium is strictly 2D so that modes with $k_{||} = 0$ remain unstable. Although these results are significant, direct application to ionospheric plasma clouds is tenuous because of the 'arbitrariness' of the parallel wavenumber ($k_{||}$). The plausible, but ad hoc, assumption that $k_{||} \sim L_z^{-1} \sim (\sigma_\perp/\sigma_{||})r_c^{-1}$, where L_z is the half-length of the cloud along $\underset{\sim}{B}$ and r_c is its radius transverse to $\underset{\sim}{B}$, leads to a stability criterion which is consistent with the observed size of barium cloud striations.

Subsequently, Drake and Huba[19] completed a fully 3D analysis of ionospheric plasma clouds. The calculation was based on a 3D elliptical waterbag cloud in which the cloud has finite extent transverse and parallel to $\underset{\sim}{B}$. The major results of this work are the following. First, the equilibrium potential consists of a polarization potential (caused by the neutral wind) and an ambipolar potential (caused by electron pressure parallel to $\underset{\sim}{B}$). The ambipolar potential causes the cloud to spin about the axis aligned with the magnetic field. The rotation rate varies with position along the length of the cloud (along $\underset{\sim}{B}$) and therefore 'shears' the cloud. This shear in the azimuthal rotation forces the $\underset{\sim}{E} \times \underset{\sim}{B}$ instability, which is nominally a flute mode ($k_{||} = 0$), to have finite $k_{||}$ and is therefore strongly stabilizing. Convective stabilization (as was found in the previous cylindrical calculation) and shear stabilization are additive and yield a stability criterion for the large-scale structuring of ionospheric plasma clouds.

The results presented in Ref. 19 are restricted to the special case $L_z/r_c = (\sigma_{||}/\sigma_{\perp})^{1/2}$. The physical nature of this special case can be understood as follows. An important feature of our previous analysis was the use of normalized coordinates which served to simplify the analysis and to demonstrate that the stability of the cloud depended only on a very limited number of parameters. The direction transverse to $\underset{\sim}{B}$ is normalized to the characteristic perpendicular scale length of the cloud r_c, while the direction parallel to $\underset{\sim}{B}$ is normalized to $\hat{L}_z = r_c(\sigma_{||}/\sigma_{\perp})^{1/2}$. In such a set of coordinates the plasma conductivity is isotropic. For typical ionospheric parameters $\sigma_{||} >> \sigma_{\perp}$ so that $L_z >> r_c$. Electrodynamically the plasma couples much better along the magnetic field than across it so that in this new coordinate system the plasma cloud is greatly reduced along $\underset{\sim}{B}$ in comparison with the original physical system. In these normalized coordinates the length of the cloud along $\underset{\sim}{B}$ is $z_c = L_z/\hat{L}_z$. In Ref. 19 $z_c = 1$ so that the cloud was a sphere in our normalized coordinates. In the present manuscript we consider the more general case of an ellipsoidal plasma cloud with z_c arbitrary. Physically, the neutral barium clouds expand radially; subsequent to photo-ionization the plasma barium cloud continues to expand along $\underset{\sim}{B}$ but its motion is inhibited transverse to $\underset{\sim}{B}$. Thus, in configuration space, barium clouds are greatly extended along $\underset{\sim}{B}$. They are ellipsoidal in appearance with the major axis aligned along $\underset{\sim}{B}$. However, in our normalized coordinate system this is not the case. When $z_c < 1$ the cloud is an ellipsoid with its major axis transverse to $\underset{\sim}{B}$; when $z_c = 1$ the cloud is spherical; and when $z_c > 1$ the cloud is an ellipsoid with its major axis parallel to $\underset{\sim}{B}$. For typical barium releases in the F-region of the ionosphere $z_c < 1$.

The organization of the paper is as follows. In the next section we present the basic equations used in the analysis. In Section III an analytical equilibrium model is derived. We derive general expressions for the polarization potential (wind driven) and the ambipolar potential (electron pressure driven). In particular, we present contour plots of the ambipolar potential, and associated flows for z_c = 1/3, 1, and 3. A stability analysis is then presented and a criterion is derived for the large-scale structuring of barium clouds. Loosely speaking, we find that clouds with $z_c << 1$ (or $L_z/r_c << (\sigma_{||}/\sigma_\perp)^{1/2}$) are more 'stable' than clouds with $z_c >> 1$ (or $L_z/r_c >> (\sigma_{||}/\sigma_\perp)^{1/2}$). In the final section we summarize our findings and apply our results to artificial ionospheric plasma clouds.

II. BASIC EQUATIONS

The general three-dimensional equations for a warm plasma cloud in a uniform magnetic field $\underset{\sim}{B} = B\,\hat{e}_z$ and a uniform background neutral wind $\underset{\sim}{V}_n = V_n\,\hat{e}_x$ (see Fig. 1) are given by[17]

$$\frac{\partial n}{\partial t} - \frac{c}{B}\nabla\phi \times \hat{z} \cdot \nabla n + \frac{\partial}{\partial z}\frac{1}{e\eta_e}\left(\frac{\partial \phi}{\partial z} - \frac{T_e}{ne}\frac{\partial n}{\partial z}\right) = 0, \tag{1}$$

$$\frac{c}{B}\frac{\nu_{in}}{\Omega_i}\nabla_\perp \cdot n\nabla_\perp\phi + D_{\perp i}\nabla_\perp^2 n + \frac{\nu_{in}}{\Omega_i}\hat{z} \times \underset{\sim}{V}_n \cdot \nabla n + \frac{\partial}{\partial z}\frac{1}{e\eta_e}\left(\frac{\partial \phi}{\partial z} - \frac{T_e}{ne}\frac{\partial n}{\partial z}\right) = 0, \tag{2}$$

where ϕ is the electrostatic potential, $\eta_e = m_e\nu_e/ne^2$ is the parallel resistivity, $\nu_e = \nu_{ei} + \nu_{en}$, $D_{\perp i} = (\nu_{in}/\Omega_i)cT_i/eB$ is the perpendicular ion diffusion coefficient, ν_{ei} is the electron-ion collision frequency and Ω_α and $\nu_{\alpha n}$ are the cyclotron and neutral collision frequencies of species α.

Equation (1) is the electron continuity equation and (1) arises from charge neutrality ($\nabla \cdot \underset{\sim}{J} = 0$). In the continuity equation the second term arises from the $\underset{\sim}{E} \times \underset{\sim}{B}$ drift while the third term arises from the parallel compression of the electron fluid. In the charge neutrality equation the first three terms arise from the ion cross field current: the first from the Pedersen conductivity, the second from diffusion associated with ion-neutral collisions and the third due to the drag between the ions and the background neutral wind. The last term in (2) again arises from the divergence of the parallel electron current. In deriving (1) and (2) we have neglected magnetic perturbations, taken T_e and T_i to be spatially uniform, assumed ν_e/Ω_e, $\nu_{in}/\Omega_i \ll 1$ so that Hall terms can be discarded, and have neglected ion parallel diffusion and perpendicular electron diffusion.

For typical F-region parameters, the parallel conductivity greatly exceeds the transverse Pedersen conductivity in the potential equation (1). As a consequence the scale lengths along the magnetic field greatly exceed those in the transverse direction. It is therefore convenient to define a set of dimensionless variables in which the conductivity is isotropic and all scale lengths become comparable. For a plasma cloud of perpendicular scale length r_c the appropriate parallel scale length is

$$\hat{L}_z = r_c \left(\Omega_e \Omega_i / \nu_e \nu_{in}\right)^{1/2}, \tag{3}$$

where for simplicity we take ν_e and ν_{in} to be spatially uniform. The dimensionless equations then become

$$\frac{\partial n}{\partial t} - \nabla\Phi \times \hat{z} \cdot \nabla n + \frac{\nu_{in}}{\Omega_i} \frac{\partial}{\partial z} \left(n \frac{\partial \Phi}{\partial z} - \Gamma \frac{\partial n}{\partial z} \right) = 0, \tag{4}$$

$$\nabla \cdot n\nabla\Phi + \partial n/\partial y - \Gamma\partial^2 n/\partial z^2 = 0, \tag{5}$$

where

$$\Phi = c\left[\phi + T_i \ln(n)/e\right]/Br_c V_n \tag{6}$$

is the normalized potential, the dimensionless parameter Γ is defined as

$$\Gamma = c(T_e + T_i)/eBV_n r_c, \tag{7}$$

and remaining dimensionless variables are defined by $tV_n/r_c \rightarrow t$, $r_c\nabla_\perp \rightarrow \nabla_\perp$, $\hat{L}_z\ \partial/\partial z \rightarrow \partial/\partial z$ and $n/n_b \rightarrow n$, where n_b is the density of the uniform background.

Because the conductivity in (5) is isotropic in our normalized variables, the scale lengths along and across the magnetic field are now comparable ($\partial/\partial z \sim \nabla_\perp$). The third term in (5) arises from the current driven by the parallel pressure gradient. This term becomes comparable in size to the first two terms in (5) when $\Gamma \gtrsim 1$.[19]

The parallel compression term in (4) is proportional to $\nu_{in}/\Omega_i \ll 1$. In our dimensionless equations all other terms are of order unity (for $\Gamma \sim 1$) so that this term is small and can be neglected. The continuity equation then simplifies to

$$\partial n/\partial t - \nabla\Phi \times \hat{z} \cdot \nabla n = 0. \tag{8}$$

The essential physics behind the neglect of the parallel compression term in (1) or (4) is easily understood. The continuity of the current [Eq. (2)] requires that the divergence of the parallel current balance the divergence of the Pedersen current. The Pedersen drift is smaller than the $\underset{\sim}{E} \times \underset{\sim}{B}$ drift [second term in (1)] by the factor ν_{in}/Ω_i. Thus, the parallel compression term in (1) and (4) is of order ν_{in}/Ω_i compared with the remaining terms.

Equations (5) and (6) depend explicitly only on the single parameter Γ. In addition, there are two important "hidden" variables: the ratio of the cloud to background density, $M = n_c/n_b$; and the characteristic scale length of the cloud parallel to the magnetic field, $z_c = L_z/\hat{L}_z$.

In the limit $\partial/\partial z = 0$, (5) and (8) are independent of r_c so that the transverse scale length is undetermined. However, when the parallel dynamics are included, the parameter $\Gamma \propto r_c^{-1}$ enters the equations. In general, we expect the plasma cloud to be unstable to the $\underset{\sim}{E} \times \underset{\sim}{B}$ instability when Γ is small. For a given cloud configuration (aspect-ratio) we expect that when Γ is sufficiently large it will dominate the remaining terms in the equations and either substantially alter or stabilize the instability. Thus, for a given cloud configuration only, clouds larger than a minimum scale size will be unstable. The calculation of this minimum cloud size was presented previously for the simplest configurations,[19] that of a sphere (an aspect-ratio of one) in our dimensionless system of equations. It was shown that the cloud was stable for $\Gamma > \Gamma_c(M)$. In the present manuscript we extend this previous work by investigating the equilibrium and stability of arbitrary aspect-ratio ellipsoids.

III. EQUILIBRIUM

We consider a waterbag cloud in the shape of an ellipsoid of radius one perpendicular to the magnetic field and length z_c along the magnetic field (see Fig. 1). The neutral wind polarizes the cloud, producing a potential Φ_{0p} which causes the cloud to drift with a velocity V_0 in the direction of the wind. In addition, an ambipolar potential Φ_{0a} develops which balances the electron pressure along the magnetic field. The ambipolar field causes the cloud to spin around its axis along $\underset{\sim}{B}$.

The equilibrium potentials can be calculated from (6) once the density profile is specified. The second term in (6) drives the polarization potential while the third drives the ambipolar potential. Since (6) is a linear functional of Φ in equilibrium, the total potential can be simply expressed as

$$\Phi_0 = \Phi_{0p} + \Phi_{0a}. \tag{9}$$

We will evaluate both of these potentials for the general ellipsoidal plasma cloud.

It is convenient to solve for the equilibrium and subsequently the stability of the cloud in spheroidal coordinates, ξ, η and ϕ. These coordinates are described in some detail in Appendix A. They are useful because surfaces of constant ξ, where ξ is the "radial variable", are either prolate or oblate ellipsoids. Thus, in these coordinates the equilibrium density n_0 is simply given by

$$n_0(\xi) = MH(\xi_c - \xi) + 1, \tag{10a}$$

where

$$\xi_c = z_c/(z_c^2 - 1)^{1/2} \qquad \text{(prolate cloud)} \qquad (10b)$$

$$= z_c/(1 - z_c^2)^{1/2} \qquad \text{(oblate cloud)} \qquad (10c)$$

is a function of the aspect ratio of the cloud and H is the Heaviside function, and M is the ratio of the cloud density to background density (i.e., n_c/n_b).

The solutions of the equilibrium equations which follow will be specifically carried out in prolate coordinates. As discussed in Appendix A, the corresponding solutions for oblate coordinates can be simply obtained by replacing ξ and ξ_c everywhere by $i\xi$ and $i\xi_c$.

A. Polarization Potential

The polarization potential is driven by the neutral wind and satisfies the equation

$$\nabla \cdot n_0 \nabla \Phi_{0p} = - \partial n_0/\partial y. \qquad (11)$$

In the vicinity of the cloud boundary, the derivatives with respect to ξ dominate those with respect to the angular variables η and Φ, and (11) simplifies to

$$\frac{\partial}{\partial \xi} n_0 \left(\xi^2 - 1\right) \frac{\partial}{\partial \xi} \Phi_{0p} = \frac{M(\xi^2 - \eta^2)}{\xi_c^2 - 1} \frac{\partial \xi}{\partial y} \delta(\xi - \xi_c), \qquad (12)$$

where $\partial\xi/\partial y$ is given in (A6) of Appendix A. In prolate ellipsoidal coordinates the center of the ellipse corresponds to $\xi = 1$ while $\xi \to \infty$ at

large distances. Integrating (12) across the δ-function, we calculate the jump conditions on Φ and its derivatives across the boundary:

$$\Phi_{0p}^{+} = \Phi_{0p}^{-}, \tag{13a}$$

$$\frac{\partial \Phi_{0p}^{+}}{\partial \xi} - (M + 1) \frac{\partial \Phi_{0p}^{-}}{\partial \xi} = M \frac{\xi_c}{\left(\xi_c^2 - 1\right)} (1 - \eta^2)^{1/2} \sin\phi, \tag{13b}$$

where $\Phi_{0p}^{\pm}$ denotes the solution for $\xi = \xi_c \pm \varepsilon$ with $\varepsilon \to 0$. Away from the cloud boundary, the potential satisfies Poisson's equation, the solutions of which are given in Appendix A. Selecting the solutions which are evanescent at large ξ and regular as $\xi \to 1$, and matching those solutions at $\xi = \xi_c$ using the jump conditions in (13), we obtain the polarization potential

$$\Phi_{0p}^{+}(\xi, \eta, \phi) = V_0 P_1^1(\eta) \sin\phi \, Q_1^1(\xi)/Q_1^1(\xi_c), \tag{14a}$$

$$\Phi_{0p}^{-}(\xi, \eta, \phi) = V_0 P_1^1(\eta) \sin\phi \, P_1^1(\xi)/P_1^1(\xi_c), \tag{14b}$$

with

$$V_0 = M \frac{\xi_c^2}{\xi_c^2 - 1} \left[(M + 1) \frac{\xi_c P_1^{1\prime}(\xi_c)}{P_1^1(\xi_c)} - \frac{\xi_c Q_1^{1\prime}(\xi_c)}{Q_1^1(\xi_c)}\right]^{-1} \tag{14c}$$

and P_1^m and Q_1^m the associated Legendre polynomials with the prime denoting a derivative with respect to the argument. The potential inside the cloud can be simplified further by noting that (see Appendix A)

$$r = (1 - \eta^2)^{1/2}(\xi^2 - 1)^{1/2}/(\xi_c^2 - 1)^{1/2}$$

$$= - P_1^1(\eta)P_1^{1\prime}(\xi)/P_1^{1\prime}(\xi_c)$$

or

$$\Phi_{0p}^{-} = - V_0 y. \tag{14d}$$

Thus, the cloud moves uniformly with a velocity

$$\underset{\sim}{V}_0 = \hat{z} \times \nabla\Phi_{0p} = V_0 \hat{x} \tag{15a}$$

in the direction of the neutral wind. In the limit of a spherical cloud ($z_c = 1$ and $\xi_c \to \infty$), V_0 can be evaluated explicitly,

$$V_0 = M/(M + 3) \tag{15b}$$

as was found previously.[19] In the limit of an extremely prolate cloud, $z_c \gg 1$ and $\xi_c \simeq 1$, V_0 can be similarly evaluated as

$$V_0 = M/(M + 2), \tag{15c}$$

which is the velocity of an infinite cylindrical cloud.

Finally, to evaluate the velocity of an oblate cloud we make the replacement $\xi_c \to i\xi_c$ in (14c) as follows:

$$V_0 = M \frac{\xi_c^2}{1 + \xi_c^2} \left[(M + 1) \frac{i\xi_c P_1^{1\prime}(i\xi_c)}{P_1^1(i\xi_c)} - \frac{i\xi_c Q_1^{1\prime}(i\xi_c)}{Q_1^1(i\xi_c)}\right]^{-1} \tag{16a}$$

For an extremely oblate cloud, $z_c \simeq \xi_c << 1$, the velocity is given by

$$V_0 = \frac{Mz_c}{2/\pi + Mz_c} \tag{16b}$$

Thus, $V_0 \to 0$ as $z_c \to 0$.

B. Ambipolar Potential

The ambipolar potential Φ_{0a} is driven by the parallel electron pressure gradient and satisfies the equation

$$\nabla \cdot n\nabla\Phi_{0a} = \Gamma\partial^2 n/\partial z^2. \tag{17}$$

Since the source on the right side of (17) is independent of the poloidal angle ϕ, Φ_{0a} is similarly independent of ϕ and the potential Φ_{0a} therefore only produces flows in the azimuthal direction, i.e., causes the cloud to spin around its z-axis.

In the vicinity of the cloud boundary, the derivatives of Φ_{0a} with respect to ξ again dominate those with respect to η, and (17) can be approximated as

$$\frac{\partial}{\partial\xi} n_0(\xi^2 - 1) \frac{\partial}{\partial\xi} \Phi_{0a} = \Gamma \frac{\xi^2 - \eta^2}{\xi_c^2 - 1} \left[\xi_{zz} n_\xi + \xi_z{}^2 n_{\xi\xi}\right], \tag{18}$$

where the subscripts z and ξ in (18) denote a derivative with respect to that variable, and the functions ξ_{zz} and ξ_z have been evaluated in Appendix A. Integrating (18) across the boundary once, we obtain the jump condition on $\partial\Phi_{0a}/\partial\xi$,

$$\frac{\partial \Phi_{0a}^{+}}{\partial \xi} - (M + 1) \frac{\partial \Phi_{0a}^{-}}{\partial \xi} = \frac{M\Gamma}{(\xi_c^2 - 1)^2} \left\{ \left[\left(\xi^2 - \eta^2 \right) \xi_z^2 \right]_\xi - \left(\xi_c^2 - \eta^2 \right) \xi_{zz} \right\}$$

$$= - M\Gamma \xi_c \frac{\partial}{\partial \eta} \frac{\eta(1 - \eta^2)}{\xi_c^2 - \eta^2} . \qquad (19)$$

Integrating (18) twice, we obtain the jump in the value of Φ_{0a}

$$\Phi_{0a}^{+} - \Phi_{0a}^{-} = - \Gamma \ln(M + 1) \frac{\left(\xi_c^2 - \eta^2 \right)}{\left(\xi_c^2 - 1 \right)^2} \xi_z^2$$

$$= - \Gamma \ln(M + 1) \eta^2 \frac{\left(\xi_c^2 - 1 \right)}{\left(\xi_c^2 - \eta^2 \right)} , \qquad (20)$$

where ξ_z and ξ_{zz} have been evaluated using the expressions given in Appendix A.

Away from the cloud boundary, the potential again satisfies Poisson's equation. Selecting the bounded solutions in the regions $\xi \gtrless \xi_c$ from the general solution in Appendix A, and matching at $\xi = \xi_c$ using the jump conditions in (19) and (20), we obtain an expression for the ambipolar potential,

$$\Phi_{0a}^{+} = \Gamma \sum_{n=2}^{\infty} b_n P_n(\eta) \frac{Q_n(\xi)}{Q_n(\xi_c)} , \qquad (21a)$$

$$\Phi_{0a}^{-} = \Gamma \sum_{n=0}^{\infty} a_n P_n(\eta) \frac{P_n(\xi)}{P_n(\xi_c)} , \qquad (21b)$$

where

$$a_n = - \left[M\beta_n + \alpha_n \ln(M + 1) \frac{\xi_c Q_n'(\xi_c)}{Q_n(\xi_c)} \right]$$

$$\times \left[(M+1)\,\frac{\xi_c P_n'(\xi_c)}{P_n(\xi_c)} - \frac{\xi_c Q_n'(\xi_c)}{Q_n(\xi_c)}\right]^{-1}, \tag{21c}$$

$$b_n = a_n - \alpha_n \ln(M+1), \tag{21d}$$

$$\alpha_n = \frac{2n+1}{2} \int_{-1}^{1} d\eta\, \frac{\xi_c^2 - 1}{\xi_c^2 - \eta^2}\, \eta^2 P_n(\eta) \tag{21e}$$

and

$$\beta_n = -\frac{2n+1}{2} \int_{-1}^{1} d\eta\, \xi_c^2\, P_n(\eta)\, \frac{\partial}{\partial \eta}\, \frac{\eta(1-\eta^2)}{\xi_c^2 - \eta^2}\,. \tag{21f}$$

Note that $a_n = b_n = 0$ for n odd since the cloud is up-down symmetric about the horizontal mid-plane. Note also that in the expression for Φ_{0a}^{+} in (21a) the sum over n extends from $n = 2$ rather than $n = 0$. The $n = 0$ contribution is zero since there is no net charge on the ellipsoid and thus no monopole contribution to the potential as $\xi \to \infty$. The corresponding solution for an oblate cloud can be obtained by simply replacing ξ_c and ξ in (21) everywhere by $i\xi_c$ and $i\xi$.

In general the potential in (21) involves an infinite sum and cannot be evaluated analytically in closed form. The exception is the limit of a spherical cloud, $\xi_c \to \infty$, for which

$$a_n = \frac{1}{3} \ln(M+1)\delta_{n0} - \frac{M - \ln(M+1)}{M + 5/2}\, \delta_{n2}, \tag{22a}$$

$$b_n = -\frac{M + (2/3)(M+1)\ln(M+1)}{M + 5/2}\, \delta_{n2}, \tag{22b}$$

in agreement with previous results.[19]

The coefficients a_n and b_n can readily be evaluated numerically for an arbitrary ellipsoid, and the potential can then be calculated. In Figs. 2a, 3a and 4a we plot the contours of constant Φ_{0a} in the r-z plane for the sphere with $z_c = 1$, a prolate ellipsoid with $z_c = 3$ and an oblate ellipsoid with $z_c = 1/3$. The solid (dashed) lines in Figs. 2-4 correspond to positive (negative) values of the potential. Associated legendre functions up to n = 24 have been retained in the sums in (21a) and (21b) to produce Figs. 3 and 4. A surface dipole layer forms on the top and bottom surfaces of the ellipsoids where the magnetic field (along z) intersects the boundary of the cloud. This dipole layer produces a potential drop at the boundary which balances the local electron parallel pressure gradient. The dipole layers at the top and bottom are oppositely directed and therefore asymptotically at large distances yield a basically quadrupole potential structure.

In Figs. 2b, 3b and 4b we plot the corresponding contours of the angular rotation rate

$$\omega_{0a} = V_{0a}/r \tag{23}$$

with

$$V_{0a} = \partial\Phi_{0a}/\partial r$$

$$= (\partial\Phi_{0a}/\partial\xi)(\partial\xi/\partial r) + (\partial\Phi_{0a}/\partial\xi)\partial\eta/\partial r, \tag{24}$$

the poloidal velocity. The functions $\partial\xi/\partial r$ and $\partial\eta/\partial r$ are given in Appendix A. In all cases the angular velocity inside the cloud is generally much smaller than that outside the cloud. For a spherical cloud, the rotation rate inside the cloud is uniform so the cloud rotates as a solid body. The rotation is nonuniform for the oblate and prolate spheroids. Outside of the cloud the fluid rotates positively at the midplane and negatively with higher velocity at the top and bottom. For a prolate spheroid, the dipole layers are sufficiently far from the midplane that the ambipolar potential in the midplane is weak and the corresponding flows are small. In the limit of extreme elongation the flows would be essentially confined to the two ends of the cloud and the central portion of the cloud would behave like a simple 2-D infinite cylinder.

In Sec. IV we will show that the rotation velocity at the midplane is important in determining the stability of 3-D plasma clouds. In Figs. 2c, 3c and 4c we therefore show the rotation rate as a function of r at the midplane. Note that the rotation rate in the cloud is constant for $z_c = 1$, falls slightly with increasing r for $z_c < 1$ and increases sharply with increasing r for $z_c > 1$. In all cases the rotation rate changes sign at the boundary, and is a maximum (in magnitude) just outside the cloud.

Finally, we emphasize that while in our normalized coordinates sample equilibria presented in Figs. 2-4 range from oblate to prolate. In the original unnormalized physical coordinates, all of these clouds would appear extremely prolate. The normalization squashes the z direction by the square root of the ratio of the perpendicular to parallel conductivity. The specific configuration of plasma clouds of interest, such as those resulting from chemical releases in the atmosphere, will be discussed in Sec. V.

IV. STABILITY ANALYSIS

In Sec. III we evaluated the equilibrium flows for a general ellipsoidal plasma cloud. We now investigate the stability of such configurations.

With the neutral wind blowing from left to right in Fig. 1, we would normally expect the cloud to be unstable to flute-like perturbations located on the backside as illustrated in Figs. 5a and 5b. The solid (dashed) lines in Fig. 5a show regions where the plasma cloud is convecting outwards (inwards) as can be seen in the midplane slice of the cloud in Fig. 5b. Along the direction of the magnetic field in Fig. 5a, the phase of the corrugations on the surface of the cloud do not vary and thus the perturbations are flutelike. In the case of a sphere, Drake and Huba[19] found that local perturbations propagate in the azimuthal direction and that the rate of propagation depends strongly on the polar angle (latitude above or below the midplane). In particular the azimuthal flows are small at the midplane and increase sharply above and below as illustrated in Fig. 5a. As a consequence the corrugations are convected as shown in Fig. 5c and lose their flute-like character - the phase of the corrugations varies strongly along $\underset{\sim}{B}$. The resulting parallel wavelength has a dissipative influence on the instability which we wish to investigate.

The equation for the plasma density can be written in terms of a displacement $\tilde{\xi}(\eta, \phi, t)$ of the cloud boundary,

$$n(\xi, \eta, \phi, t) = MH(\tilde{\xi} + \xi_c - \xi) + 1. \qquad (25)$$

Thus, the perturbation of the density is given by

$$\tilde{n} = - \tilde{\xi} \, \partial n_0 / \partial \xi, \tag{26}$$

where we work in the frame of reference of the moving cloud so that $n_0 = n_0(\xi)$ is time independent. Since the plasma flow is incompressible, the density perturbation in (26) simply arises from the displacement of the initial cloud boundary and therefore vanishes away from the boundary. Inserting (25) into the continuity equation (8) and linearizing, we obtain an equation for the time evolution of $\tilde{\xi}$,

$$\frac{\partial \tilde{\xi}}{\partial t} + \left(\nabla\phi \times \hat{z} \cdot \nabla\xi\right)\left(\tilde{\xi}\Phi_{0c\xi}\right)_\phi - \Phi_{0c\eta}\left(\nabla\eta \times \hat{z} \cdot \nabla\phi\right)\tilde{\xi}_\phi + \left(\nabla\phi \times \hat{z} \cdot \nabla\xi\right)\tilde{\Phi}_\phi = 0, \tag{27}$$

where $\tilde{\Phi}$ is the perturbed potential, the subscripts ϕ, η and ξ denote a partial derivative with respect to that variable, and

$$\Phi_{0c} = \Phi_0 + V_0 y \tag{28}$$

is the equilibrium potential in the frame of the cloud.

We then linearize the charge neutrality equation (6) to obtain an equation for the perturbed potential $\tilde{\Phi}$

$$\nabla \cdot n_0 \nabla\tilde{\Phi} - \nabla \cdot \tilde{\xi} n_{0\xi} \nabla\Phi_{0c} - (1 - V_0)(\tilde{\xi} n_{0\xi})_y + r(\tilde{\xi} n_{0\xi})_{zz} = 0. \tag{29}$$

Away from the cloud boundary, the second, third and fourth terms in (29) vanish since $n_{0\xi} = 0$ so that the potential satisfies Poisson's equation,

$$\nabla^2\tilde{\Phi} = 0. \tag{30}$$

Thus, the stability calculation can, in principle, be completed by solving (30) inside and outside the cloud and deriving a set of jump conditions for $\tilde{\Phi}$ and its derivatives across the boundary to match the inner and outer solutions.

To avoid overly complicating the equations we will first simplify the problem and retain only the dominant contributions to the equations. Specifically, we expect that flute-like perturbations with $\partial/\partial\phi >> \partial/\partial\eta$ will be unstable. We therefore limit the stability calculation to perturbations for which $\partial/\partial\phi >> \partial/\partial\eta >> 1$. In this limit the ϕ dependence of $\tilde{\xi}$ and $\tilde{\Phi}$ can be represented by the eikonal $\tilde{\Phi}$, $\tilde{\xi} \sim \exp[iS(\phi)]$ where

$$\partial S/\partial\phi \equiv m(\phi), \tag{31}$$

with m the local mode number. As discussed in the beginning of this section, the variation of the equilibrium with η then forces $\partial/\partial\eta \neq 0$ and we find that, as in the case of the sphere, the modes are localized in a region $\eta \sim m^{-1/2}$ around the midplane of Fig. 5 where the shearing of the striations is weakest. In particular, we find that $\partial/\partial\eta \sim m^{1/2} << \partial/\partial\phi \sim m$ and the mode retains its basic flute character.

Away from the boundary, $\tilde{\Phi}$ satisfies (30), which in prolate coordinates (A4) can be written as

$$\frac{\partial}{\partial \xi}(\xi^2 - 1)\frac{\partial \tilde{\Phi}}{\partial \xi} - m^2 \frac{\xi^2}{\xi^2 - 1}\tilde{\Phi} = 0, \tag{32}$$

where $\partial^2\tilde{\Phi}/\partial\eta^2$ has been neglected compared with the second term in (32) and we have taken $\eta << 1$ for modes localized around the midplane. The solution of (32) for $m >> 1$ which are well behaved as $\xi \to 1$ and $\xi \to \infty$ are strongly localized around the cloud boundary at $\xi = \xi_c$,

$$\tilde{\Phi} \sim \exp[\pm k(\xi - \xi_c)/\xi_c]$$

with the $\pm$ denoting outside and inside the cloud, respectively, and

$$k = m\xi_c^2/(\xi_c^2 - 1) \tag{33}$$

the local radial wavevector. The final form of the potential perturbation is given by

$$\tilde{\Phi} = \tilde{\Phi}^{\pm}(\eta)\exp\left[iS(\phi)\right]\exp\left[\mp k\left(\xi - \xi_c\right)/\xi_c\right]\exp(\gamma t), \tag{34}$$

where γ is the local growth rate. The displacement is given by the simple expression

$$\tilde{\xi}(\eta, \phi) = \tilde{\xi}\exp[iS(\phi)]\exp(\gamma t), \tag{35}$$

The evaluation of the jump conditions on $\tilde{\Phi}$ at the cloud boundary is complicated by the fact that the potential $\tilde{\Phi}$ is singular at the cloud boundary. This can be seen by noting that the term proportional to Γ in

(29) has three derivatives acting on n_0. Thus, even after integrating (29) twice with respect to ξ, we find

$$\tilde{\Phi} \sim \Gamma\, \tilde{\xi} n_{0\xi},$$

which is singular at the boundary. This result should not be surprising. The equilibrium potential Φ_{0c} has a jump discontinuity at the boundary. The displacement of the equilibrium potential therefore produces a perturbed potential

$$\tilde{\Phi} \sim \tilde{\xi}\, \partial\Phi_{0c}/\partial\xi$$

which is singular. The singularity in the perturbed potential can be eliminated by subtracting this contribution from $\tilde{\Phi}$, by defining a new dependent variable

$$\hat{\Phi} = \tilde{\Phi} + \tilde{\xi}\, \partial\Phi_{0c}/\partial\xi. \tag{36}$$

The continuity equation then simplifies to

$$\frac{\partial\tilde{\xi}}{\partial t} + (\nabla\phi \times \hat{z} \cdot \nabla\xi)\hat{\Phi}_\phi - \Phi_{0c\eta}(\nabla\eta \times \hat{z} \cdot \nabla\phi)\hat{\xi}_\phi = 0 \tag{37}$$

and the charge neutrality equation becomes

$$\nabla \cdot n_0\nabla\hat{\Phi} - \nabla \cdot n_0\nabla\tilde{\xi}\Phi_{0c\xi} - \nabla \cdot \tilde{\xi} n_{0\xi}\nabla\Phi_{0c}$$

$$- \left(1 - V_0\right)\left(\tilde{\xi} n_{0\xi}\right)_y + \Gamma\left(\tilde{\xi} n_{0\xi}\right)_{zz} = 0 \tag{38}$$

The second and fifth terms in (38) now cancel to lowest order (compare with the equilibrium equation for Φ_{0c}) so that $\hat{\Phi}$ remains finite at the cloud boundary.

Around the midplane ($\eta \simeq 0$), the third term in (37) is small and can be neglected and the second term simplifies since $\nabla\phi \times \hat{z} \cdot \nabla\xi \simeq \xi_r \simeq (\xi_c^2 - 1)/\xi_c$ so that

$$\gamma\tilde{\xi} + \xi_r\hat{\Phi}_\phi = 0. \tag{39}$$

Since this equation must be satisfied on both sides of the cloud boundary, $\hat{\Phi}$ must be continuous at the boundary or

$$\tilde{\Phi}^+ + \tilde{\xi}\Phi^+_{0c\xi} = \tilde{\Phi}^- + \tilde{\xi}\Phi^-_{0c\xi}. \tag{40}$$

The evaluation of the jump in $\partial\hat{\Phi}/\partial\xi$ across the boundary is more difficult. Equation (38) is first multiplied by $(\xi^2 - \eta^2)$ and integrated across the boundary. The details of the calculation are presented in Appendix B. The result is

$$\left(\xi_c^2 - 1\right)^2\left(n_0\tilde{\Phi}_\xi\right)^+_- + \left(1 - V_0\right)M\xi_c^2\cos\phi\ \tilde{\xi}_\phi$$

$$+ M\Gamma\left(\xi_c^2 - 1\right)\eta^2\ \tilde{\xi}_{\phi\phi} - M\Gamma\left(\xi_c^2 - 1\right)\tilde{\xi}_{\eta\eta} = 0. \tag{41}$$

Note that the third term on the left side of (41) is proportional to η^2 and might be considered small. It is multiplied by $\partial^2/\partial\phi^2$ which is large and it must therefore be retained. Equation (41) can now be reduced to a single second order differential equation for the angular dependence of $\tilde{\xi}(\eta)$ by inserting $\tilde{\Phi}$ and $\tilde{\xi}$ in (34) and (35) into (41) and eliminating $\tilde{\Phi}^\pm$ using (39) and (40),

$$\frac{\partial^2}{\partial\eta^2}\tilde{\xi} + (1 + i\delta)m^2\eta^2\tilde{\xi} + i\,\frac{M+2}{M\Gamma}\,\frac{\xi_c^{\,2}}{\xi_c^{\,2}-1}\left(\gamma - \gamma_0\cos\phi + i\omega_0\right)\tilde{\xi} = 0, \quad (42)$$

where

$$\gamma_0 = m\left(1 - V_0\right)M/(M+2), \quad (43)$$

$$\omega_0(\phi) = m\left[\Phi^{+}_{0cr}(\eta = 0) + (M+1)\Phi^{-}_{0cr}(\eta = 0)\right]/(M+2), \quad (44)$$

and δ arises from small parallel diffusion in the continuity equation. This term is necessary to identify the bounded eigenmodes of (42). Before solving the equation, we can examine the local dispersion relation by simply ignoring $\partial^2/\partial\eta^2$ in (42),

$$\gamma = \gamma_0\cos\phi - i\omega_0 + im^2\,\frac{M\Gamma}{M+2}\,\frac{\xi_c^{\,2}-1}{\xi_c^2}\,(1 + i\delta)\eta^2. \quad (45)$$

The term proportional to γ_0 in (45) represents the local growth of the $\underset{\sim}{E} \times \underset{\sim}{B}$ instability for the elliptical plasma cloud. The instability grows on the backside of the cloud ($\cos\phi > 0$) and is proportional to the relative drift of the neutral wind and the plasma cloud. The second term in the right hand side of (45) arises from the azimuthal fluid flow near the cloud boundary which convects the local perturbation in ϕ and therefore produces a finite frequency ω_0. These flows vary with the angle η and therefore the propagation rate of local perturbations also varies with η. As discussed earlier, such variation of the propagation rate leads to shearing of the flute perturbations, which we expect to be stabilizing. However, the angular variation of the propagation velocity arising from the fluid flows is small compared with that arising from the

third term on the right side of (45) so the fluid flows are simply evaluated at $\eta = 0$.

The third term in the right hand side of (45) also causes local perturbations to propagate. This term represents the local diamagnetic frequency for this geometry. In an earlier investigation of the stability of an infinite cylindrical plasma cloud, Drake and Huba[19] showed that perturbations with non-zero parallel wavevector k_z have a diamagnetic frequency,

$$\omega_* = - \frac{M}{M + 2} \Gamma k_z^2, \tag{46}$$

where the result has been written in our system of dimensionless units. In the present ellipsoidal cloud,

$$k_z^2 \sim \xi_z^2 \, \partial^2/\partial\xi^2 \sim \xi_z^2 k^2/\xi_c^2$$

$$\sim m^2\eta^2\left(\xi_c^2 - 1\right)/\xi_c^2, \tag{47}$$

where k is given in (33) and ξ_z in (A7) and we have taken the limit $\eta \ll 1$. Substituting (47) into (46) we obtain the propagation frequency ω_*,

$$\omega_* = - m^2 \frac{M\Gamma}{M + 2} \frac{\xi_c^2 - 1}{\xi_c^2} \eta^2 \tag{48}$$

which is precisely the frequency given in (45). An important feature of (48) is that the frequency varies as η^2. This dependence on η arises from the geometry of the configuration. The derivative with respect to ξ is large, $\partial/\partial\xi \sim m$ but $\nabla\xi$ is orthogonal to $\hat{z}$ at the midplane, $\nabla z \cdot \nabla\xi \sim \xi_z \sim \eta$. The η^2 arises from the projection of $\nabla\xi$ along the magnetic field.

Finally, we emphasize that ω_* is important even though it scales as η^2 because it is also proportional to m^2. Specifically, $\omega_* \sim 1$ when $\eta \sim m^{-1} \ll 1$. This rapid variation of the mode propagation velocity with η causes shearing of the striations and is strongly stabilizing, as we will now demonstrate.

The bounded solution to (42) is given by

$$\tilde{\xi} \sim \exp\left[im\left(1 + i\delta/2\right)\eta^2/2\right] \tag{49}$$

and yields the eigenvalue

$$\gamma = \gamma_0\cos\phi - m\frac{M\Gamma}{M+2}\frac{1}{z_c^2} - i\omega_0, \tag{50}$$

where ξ_c has been eliminated in favor of the cloud elongation z_c using (11a). The growth rate γ in (50) is valid for both oblate and prolate clouds. The solution for $\tilde{\xi}$ in (49) becomes increasingly oscillatory as η increases, as a result of the shearing of the striations depicted in Fig. 5. The associated damping is given by the second term in the right side of (50). For a spherical cloud, $z_c = 1$, and the growth rate in (50) reduces to that presented previously.[19] As the cloud becomes prolate, $z_c > 1$ and the damping rate in (50) is reduced. The limit of $z_c \to \infty$, that of an infinte cylinder, the damping is zero, as expected. For an oblate cloud, $z_c < 1$ and the damping increases. On the basis of these results, we would expect oblate plasma clouds to be more stable than prolate clouds.

As mentioned previously the frequency ω_0 arises from azimuthal fluid flows at the cloud boundary and since the polarization potential Φ_{0p} is proportional to $\sin\phi$ [see (14)], ω_0 is generally a strong function of ϕ. In previous investigations of the stability of a cylindrical waterbag

cloud to modes with $k_z \neq 0$,[18] it was shown that growing modes localized an angle ϕ_0 where $\omega_0 = 0$. At locations where $\omega_0 \neq 0$, perturbations convect to the stable front side of the plasma cloud where they are damped. In the present investigation the modes are not localized in the azimuthal angle ϕ. Nevertheless, we expect that perturbations growing at locations ϕ_0 where $\omega_0 = 0$ will grow the finite amplitudes while those growing to where $\omega_0 \neq 0$ will be convectively stabilized.

When $\Gamma << 1$, the ambipolar potential Φ_{0a} is small, and ω_0 simply arises from the flow of the background plasma past the cloud. In this case there is a stagnation point in the flow at $\phi = 0$ so that $\omega_0 = 0$ at that point. More generally, when $\Gamma \sim 1$, the ambipolar flows which are independent of ϕ, balance the polarization flows at a finite angle ϕ.

For Γ sufficiently small, $\phi_0 \simeq 0$ and the local growth rate from (50) is given by $\gamma \simeq \gamma_0$. As Γ increases, ϕ_0 is generally non-zero and the local growth rate where $\omega_0(\phi_0) = 0$ is given by

$$\gamma = \gamma_0 \cos\phi_0 - m \frac{M\Gamma}{M + 2} \frac{1}{z_c^2} . \tag{51}$$

For Γ sufficiently large, the damping in (51) exceeds the driving term and the plasma cloud is stable. Since $\gamma_0 \propto m$, the stability boundary is independent of m; therefore, all azimuthal mode numbers m are stabilized at the same value of Γ. The equations for Γ_c, the critical value for Γ for stability, are given by

$$\Gamma_c = z_c^2 \left(1 - V_0\right) \cos\phi_0, \tag{52a}$$

where

$$\omega_0\left(\phi_0, \Gamma_c, M, z_c\right) = 0 \tag{52b}$$

determines ϕ_0. The cloud is unstable for $\Gamma < \Gamma_c$ and stable for $\Gamma > \Gamma_c$. In Figs. 6 and 7 we show Γ_c and ϕ_0 versus M for $z_c = 1$, 3 and 1/3. In all cases, ϕ_0 decreases from a positive to a negative value as M increases. The decrease of Γ_c with M occurs because V_0 approaches 1 for large M, the cloud velocity approaches the neutral wind velocity. The driving force of the $\underset{\sim}{E} \times \underset{\sim}{B}$ instability, which is proportional to the slip velocity of the neutral wind and plasma cloud, becomes small [$\Gamma_c \sim 1 - V_0$ in (52a)]. Comparing all three figures, the threshold Γ_c increases strongly with increasing elongation of the cloud. Thus, as expected, oblate clouds are more stable than spherical clouds, which are more stable than prolate clouds.

V. SUMMARY AND DISCUSSION

The equilibrium and stability of three dimensional ionospheric plasma clouds has been investigated. The motivation for the present paper is to develop a theoretical model of plasma clouds for an arbitrary ellipsoidal cross-section (i.e., $z_c \neq 1$ in Fig. 1). This calculation represents a generalization of the analysis presented in Drake and Huba[19] which is valid only for the spherical case (i.e., $z_c = 1$).

In Section II we presented the fundamental equations used in the analysis [(6) and (8)]. It is important to note that these are valid in the regime $\partial/\partial t \ll \nu_{in} \ll \Omega_i$. These assumptions allow ion inertia and ion diffusion parallel to $\underset{\sim}{B}$ to be neglected. This regime is typical of barium clouds released in the F region of the ionosphere. For example, barium clouds released at ~ 180 km have $\partial/\partial t \sim 0.1$ sec^{-1}, $\nu_{in} \sim 1$ sec^{-1}, and $\Omega_i \sim 20$ sec^{-1}.

In Section III an equilibrium solution to (6) and (8) was derived. The analysis is carried out using a prolate and oblate ellipsoidal coordinate system. We consider a waterbag density profile: $n = n_c + n_b$ inside the cloud and $n = n_b$ outside the cloud where $n_{c,b}$ are the cloud and background densities, respectively. The equilibrium potentials consists of two parts: the polarization potential (which is driven by the neutral wind), and the ambipolar potential (which is driven by the parallel electron pressure). In the cloud frame, the polarization potential causes the background plasma to flow around the cloud transverse to $\underset{\sim}{B}$. The ambipolar potential produces flows only in the azimuthal direction, i.e., it causes the cloud and background plasma to rotate about the z-axis (see Figs. 2-4). The azimuthal rotation rate just inside and outside of the cloud varies strongly with position on the surface of the cloud. The variation of these azimuthal flows causes 'shearing' of the conventional flute perturbations of the $\underset{\sim}{E} \times \underset{\sim}{B}$ instability and is stabilizing.

In Section IV a stability analysis of the ellipsoidal waterbag equilibrium was performed. The calculation is in the 'long wavelength limit' because of the waterbag density profile used, i.e., $\lambda >> L_n$ where λ is the perturbation wavelength and L_n is the density gradient scale length at the cloud boundary (which is effectively 0). This limit corresponds to the observed structuring scale lengths associated with barium clouds. The major result of this section is the marginal stability criterion embodied in (52). There are two components which make up this criterion. First, (52b) requires $\omega_0 = 0$ where ω_0 [given in (44)] is the local mode frequency. For $\omega_0 = 0$ the mode remains stationary on the unstable 'backside' of the cloud, and does not convect to the stable 'frontside'. Second, (52a) results from the requirement that $\gamma = 0$ where γ [given in (51)] is the growth rate. The cloud is stable for $\Gamma = c(T_e + T_i)/eBV_n r_c >$

Γ_c and is unstable for $\Gamma < \Gamma_c$, where the solution of the dispersion relation in (52) yields $\Gamma_c = \Gamma_c(z_c,M)$. In Fig. 6, we plot Γ_c versus M for several values of z_c; in Fig. 7 we plot the corresponding values of ϕ_0, the azimuthal angle at which $\omega_0 = 0$ at marginal stability.

Two separate physical effects combine to produce the stability criterion presented in (52) and Figs. 6 and 7. First, the condition that the mode not propagate ($\omega_0 = 0$) forces the mode to localize at a finite azimuthal angle ϕ_0 which is generally nonzero, as can be seen in Fig. 7. The non-propagating solution results when the diamagnetic propagation of the mode balances the propagation caused by background azimuthal flows and has been discussed in detail in Ref. 18. The localization of the mode at a finite value of ϕ_0 weakens the instability since the neutral wind is not blowing directly across the density gradient when $\phi \neq 0$ (see Fig. 1). Complete stabilization of the mode by this mechanism requires $\phi \geq \pi/2$ so that the mode is no longer localized on the backside of the cloud. This does not happen for the ellipsoidal clouds investigated here since in Fig. 7, $\phi_0 \lesssim \pi/4$.

The second stabilizing mechanism results from the "shearing" of the striations which is illustrated in Fig. 5. The usual $\underset{\sim}{E} \times \underset{\sim}{B}$ instability causes striations to form on the backside of the cloud as shown in Figs. 5a and 5b. The striations are aligned parallel to the magnetic field so that parallel currents, which are stabilizing, are minimized. In a 3-D ellipsoidal plasma cloud the azimuthal plasma flows associated with the ambipolar and polarization potentials, and diamagnetic propagation cause the striations to propagate azimuthally. However, the propagation rate is not uniform and, in fact, increases away from the midplane ($z = 0$) as indicated by the azimuthal arrows in Fig. 5a. As a result, the striations begin to twist or shear as illustrated in Fig. 5c. As a result, the

striations are no longer flutes but are forced to have $k_z \neq 0$. This effect is stabilizing and gives rise to an explicit damping rate [see (51)] which scales as Γ/z_c^2. Generally, both shear stabilization and convective stabilization combine to produce Γ_c shown in Fig. 6. The exception is the set of points with $\phi_0 = 0$ in Fig. 7, where the stabilization of the mode arises entirely from shear damping.

To obtain a simple analytic expression for Γ_c from the dispersion relation in (52) is difficult because ω_0, given in (44), depends on the ambipolar potential which cannot be calculated analytically. However, for the entire range of M and z_c presented in Fig. 7, $|\phi_0| \lesssim \pi/4$ so that cos $\phi_0 \sim 1$ in (52a). The influence of convection on the stability of the mode is therefore weak. An approximate dispersion relation can therefore be obtained by taking cos $\phi_0 \sim 1$ in (52a), leaving

$$\Gamma_c/z_c^2 \simeq 1 - V_0. \qquad (53)$$

The left side of (53) represents the shear damping of the striations and the right side represents the driving force of the instability, proportional to the slip velocity between the neutral wind (one in our normalized units) and plasma cloud (V_0). The cloud velocity V_0, given in (14c) and (16a), can be evaluated explicitly as

$$V_0 = M/(M + 2) \qquad z_c >> 1, \qquad (54a)$$

$$V_0 = M/(M + 3) \qquad z_c = 1, \qquad (54b)$$

$$V_0 = Mz_c/(2/\pi + Mz_c) \qquad z_c << 1. \qquad (54c)$$

For $z_c \gg 1$,

$$\Gamma_c/z_c^2 = 2/(M + 2). \tag{55}$$

The driving term reduces to the usual cylindrical result, as it should. For z_c large Γ_c must be very large in order to stabilize the cloud. For $z_c \ll 1$,

$$\Gamma_c/z_c^2 = (2/\pi)/(2/\pi + Mz_c), \tag{56}$$

and the Γ_c is very small. For M large both (55) and (56) yield $\Gamma_c \sim M^{-1}$, consistent with Fig. 6. For M large, the relative slip velocity of the neutral wind and plasma cloud is small so that weak damping is sufficient to stabilize the cloud. Thus, we conclude that short clouds ($z_c \ll 1$) with high M are easiest to stabilize while long clouds ($z_c \gg 1$) with low M are the most difficult to stabilize.

We now apply these results to the structuring of F region barium releases. It has been observed that barium clouds develop field-aligned striations because of the $\underset{\sim}{E} \times \underset{\sim}{B}$ instability, and effectively break up into smaller 'clouds'. These smaller 'clouds' (or 'fingers') also undergo structuring and break up into even smaller 'clouds'. This process is referred to as bifurcation and, in principal, could continue down to scale lengths associated with 'dissipative' effects (e.g., electron diffusion, finite Larmor radius effects). However, observations indicate that the striations 'freeze' at scale sizes substantially larger than the 'dissipation' scale lengths. For example, typical ionospheric parameters for barium clouds released at ~ 180 km are $T_e \simeq T_i \simeq 0.1$ eV, $B \simeq 0.3$ G, $V_n \simeq 100$ m/sec, $n_c \simeq 10^6 - 10^7$ cm^{-3}, and $n_b \simeq 10^5$ cm^{-3}. For these parameters

the dissipation scale lengths are $\lesssim$ 12 m while the 'freezing' radius of clouds is ~ 200 m.[28] Applying (52) to ionospheric releases, we compute the value of Γ based on the observed freezing scale radius of ~ 200 m. For the parameters quoted above we find that $\Gamma \simeq 0.3$. Now, assuming that $L_z \sim 15$ km, $r_c \sim 200$ m, $\Omega_e \sim 6 \times 10^6$ sec^{-1}, $\Omega_i \sim 20$ sec^{-1}, $\nu_i \sim 1$ sec^{-1}, $\nu_e \sim 2 \times 10^3$ sec^{-1} we find that $\hat{L}_z = r_c(\Omega_e\Omega_i/\nu_e\nu_{in})^{1/2} \simeq 250\, r_c \simeq 50$ km. Thus, $z_c = L_z/\hat{L}_z \simeq 1/3$. We see then from Fig. 6 that $\Gamma \sim 0.3 > \Gamma_c$ for all M. A cloud of radius 200 m is therefore stable, consistent with observations. Thus, the convective or shear stabilization of barium striations in three dimensions appears to be a plausible explanation of the freezing phenomenon.

Although three dimensional effects can account for the freezing of striations, it is not clear what role they play in the determination of the freezing scale size. During the initial evolution of an ionospheric barium cloud, the cloud is clearly not in equilibrium. In the presence of a neutral wind or ambient electric field, the cloud steepens on one side and develops a sharp density gradient. This 'steepened' side can become unstable to the $\underset{\sim}{E} \times \underset{\sim}{B}$ instability, producing the observed striations. During this initial structuring process, the waterbag cloud model used in this paper is not appropriate, and hence, the stability analysis is not applicable. This is not to say that 3D effects are not important during the onset of instability, but rather than the theory and results presented in this paper cannot be used. However, after the initial structuring of the cloud, the smaller clouds or 'fingers' can evolve into waterbag-like equilibrium, and they are stable to subsequent structuring because of 3D effects. In fact, recent 3D numerical simulation results support this hypothesis.[25]

ACKNOWLEDGMENT

We thank Ralph Kilb for a critical review of the manuscript. This research has been supported by the Defense Nuclear Agency.

APPENDIX A: Prolate and Oblate Spheroidal Coordinates

The equilibrium and stability of a prolate (oblate) ellipsoidal plasma cloud can be calculated most easily in prolate (oblate) spheroidal coordinates, ξ, η and ϕ.

In prolate spheroidal coordinates the "radial" variable $1 < \xi < \infty$ satisfies the equation

$$\frac{z^2}{\xi^2} + \frac{r^2}{\xi^2 - 1} = \frac{1}{\xi_c^2 - 1}, \tag{A1}$$

where z, r and ϕ are cylindrical coordinates. Surfaces of constant ξ are nested prolate ellipsoids which are extremely elongated along z for $\xi \gtrsim 1$ and approach spheres as $\xi \to \infty$. The surface of our ellipsoidal plasma cloud is defined by $\xi = \xi_c$, corresponding to a semi-minor axis of unity and a semi-major axis, z_m, given by

$$z_m = \xi_c / \left(\xi_c^2 - 1\right)^{1/2}. \tag{A2}$$

Thus, the aspect ratio of the ellipsoidal cloud is determined by the parameter ξ_c. For ξ_c large, the cloud is nearly spherical, while for $\xi_c \gtrsim 1$, the cloud is highly elongated along z.

The angular variable $-1 \leq \eta \leq 1$ satisfies the equation

$$\frac{z^2}{\eta^2} - \frac{r^2}{1 - \eta^2} = \frac{1}{\xi_c^2 - 1}. \tag{A3}$$

It has a value +1, 0, -1 along the positive z axis, the midplane ($z = 0$) and along the negative z axis, respectively. The azimuthal angle ϕ is the same as in cylindrical coordinates.

An important feature of spheroidal coordinates is that solutions of Laplace's equation in these variables are separable,

$$\nabla^2\Phi = \frac{\left(\xi_c^{\,2} - 1\right)}{\xi^2 - \eta^2}\left[\frac{\partial}{\partial\xi}\left(\xi^2 - 1\right)\frac{\partial}{\partial\xi} + \frac{\partial}{\partial\eta}\left(1 - \eta^2\right)\frac{\partial}{\partial\eta}\right.$$

$$\left. + \left(\frac{1}{\xi^2 - 1} + \frac{1}{1 - \eta^2}\right)\frac{\partial^2}{\partial\phi^2}\right]\Phi = 0. \qquad \text{(A4)}$$

Thus, the general solution of (A4) can be written as

$$\Phi(\xi, \eta, \phi) = \sum_{l,m} P_l^{\,m}(\eta)\left[a_{l,m}P_l^{\,m}(\xi) + b_{l,m}Q_l^{\,m}(\xi)\right]$$

$$\times \left[c_m \cos(m\phi) + d_m \sin(m\phi)\right], \qquad \text{(A5)}$$

where P_l^m and Q_l^m are the associated Legendre polynomials. The solution of (A4) proportional to $Q_l^{\,m}(\eta)$ has been eliminated since it is singular at $\eta = \pm 1$.

The equilibrium/stability calculation of an ellipsoidal cloud requires the evaluation of a number of functions which can be readily calculated using (A1) and (A3),

$$\frac{\partial\xi}{\partial y} = \frac{\xi\left(\xi^2 - 1\right)^{1/2}\left(1 - \eta^2\right)^{1/2}\left(\xi_c^{\,2} - 1\right)^{1/2}}{\left(\xi^2 - \eta^2\right)}\sin\phi, \qquad \text{(A6)}$$

$$\frac{\partial\xi}{\partial z} = \frac{\eta\left(\xi^2 - 1\right)\left(\xi_c^{\,2} - 1\right)^{1/2}}{\left(\xi^2 - \eta^2\right)}, \qquad \text{(A7)}$$

$$\frac{\partial^2 \xi}{\partial z^2} = \frac{\xi\left(\xi^2 - 1\right)\left(1 - \eta^2\right)}{\left(\xi^2 - \eta^2\right)^3}\left(\xi^2 + 3\eta^2\right)\left(\xi_c{}^2 - 1\right), \tag{A8}$$

$$\partial\xi/\partial r = \xi\left(\xi^2 - 1\right)^{1/2}\left(\xi_c{}^2 - 1\right)^{1/2}\left(1 - \eta^2\right)^{1/2}/\left(\xi^2 - \eta^2\right), \tag{A9}$$

$$\partial\eta/\partial r = -\eta\left(\xi^2 - 1\right)^{1/2}\left(\xi_c{}^2 - 1\right)^{1/2}\left(1 - \eta^2\right)^{1/2}/\left(\xi^2 - \eta^2\right), \tag{A10}$$

$$\partial\eta/\partial z = \xi\left(\xi_c{}^2 - 1\right)^{1/2}\left(1 - \eta^2\right)/\left(\xi^2 - \eta^2\right)^{1/2}. \tag{A11}$$

Oblate spheroidal coordinates, ξ, η, ϕ are similar to prolate spheroidal coordinates. The analogous Eqs. (A1) - (A11) for oblate spheroidal coordinates can be obtained by simply replacing ξ and ξ_c by $i\xi$ and $i\xi_c$, respectively, in these equations. For example, (A1) transforms to

$$\frac{z^2}{\xi^2} + \frac{r^2}{\xi^2 + 1} = \frac{1}{\xi_c{}^2 + 1}, \tag{A12}$$

for oblate coordinates. In oblate spheroidal coordinates the "radial" variable ξ extends over the range $0 \leq \xi \leq \infty$. Surfaces of constant ξ approach discs as $\xi \to 0$ and spheres as $\xi \to \infty$. The surface of the plasma cloud is again defined by $\xi = \xi_c$ and has a semi-major axis of unity with a semi-minor axis (along z) given by

$$z_m = \xi_c/\left(\xi_c{}^2 + 1\right)^{1/2}. \tag{A13}$$

APPENDIX B: Jump Conditions at the Cloud Boundary

In this appendix we evaluate the jump in $\partial\hat{\Phi}/\partial\xi$ across the cloud boundary. While this calculation can be completed without approximation, we avoid presenting excessive algebra by considering only the case $\partial/\partial\phi \sim m \gg \partial/\partial\eta \sim \eta^{-1} \sim m^{1/2} \gg 1$ where the local azimuthal mode number m is defined in (31). Terms which are small in this ordering are discarded.

The volume element in ellipsoidal coordinates is $(\xi^2 - \eta^2)d\xi d\eta$. Thus, to calculate the jump in $\partial\hat{\Phi}/\partial\xi$, we multiply (38) by ξ^2/η^2 and integrate across the boundary. The integral of the first term in (38), evaluated in ellipsoidal coordinates, is given by

$$I\ \nabla\cdot n_0\nabla\hat{\Phi} = \left(\xi_c^{\,2} - 1\right)\int_{\xi_c^-}^{\xi_c^+}\left[\frac{\partial}{\partial\xi}\, n_0\left(\xi^2 - 1\right)\frac{\partial}{\partial\xi} + n_0\,\frac{\partial}{\partial\eta}\left(1 - \eta^2\right)\frac{\partial}{\partial\eta}\right.$$

$$\left. + n_0\left(\frac{1}{\xi^2 - 1} + \frac{1}{1 - \eta^2}\right)\frac{\partial^2}{\partial\phi^2}\right]\hat{\Phi}. \qquad \text{(B1)}$$

where I is shorthand notation for the integral operator

$$I = \int_{\xi_c^-}^{\xi_c^+} d\xi\left(\xi^2 - \eta^2\right)$$

with $\xi_c^{\pm} = \xi_c \pm \varepsilon$ with ε small. Since $\hat{\Phi}$ is not singular at the boundary, only the first term in (B1) survives,

$$I\ \nabla\cdot n_0\nabla\hat{\Phi} = \left(\xi_c^{\,2} - 1\right)^2\left(n_0\hat{\Phi}_\xi\right)^+. \qquad \text{(B2)}$$

From (33) and (34), we find that $\hat{\Phi}_\xi \sim m$ so that the expression in (B2) has a magnitude $m >> 1$. Only terms of this magnitude are retained as the integrals over the remaining terms in (38) are carried out. The integral of the second term in (38) is given by

$$I\ \nabla\cdot n_0 \nabla\ \hat{\xi}\ \Phi_{0c\xi} = \left(\xi_c^{\,2} - 1\right) \int_{\xi_c^-}^{\xi_c^+} d\xi$$

$$\times\ \left[\frac{\partial}{\partial\xi}\, n_0\left(\xi^2 - 1\right) + n_0\, \frac{\partial}{\partial\eta}\left(1 - \eta^2\right) \frac{\partial}{\partial\xi} + n_0\left(\frac{1}{\xi^2 - 1} + \frac{1}{1 - \eta^2}\right) \frac{\partial^2}{\partial\phi^2}\right]\ \tilde{\xi}\ \Phi_{0c\xi}. \tag{B3}$$

In the equilibrium Φ_{0c} undergoes a jump at the cloud boundary so that $\partial\Phi_{0c}/\partial\xi$ is singular. The second and third terms in (B3) therefore yield finite contributions. For $\partial/\partial\phi >> \partial/\partial\xi >> 1$, the third term in (B3) dominates. The angular portion of $\Phi_{0c\xi}$ arises only from the ambipolar field which is independent of ϕ so that (B3) simplifies to

$$I\nabla\cdot n_0 \nabla\tilde{\xi} I_{0c\xi} = \xi_c^{\,2}\ \tilde{\xi}_{\phi\phi} \int_{\xi_c^-}^{\xi_c^+} d\xi\ n_0 \Phi_{0c\xi} \tag{B4}$$

where we have taken $\eta << 1$. An expression for $n_0\Phi_{0c\xi}$ can be obtained by integrating the equilibrium equation for Φ_0 in (18)

$$n_0\Phi_{0c\xi} = \Gamma\ \xi_z^{\,2} n_{0\xi} \xi_c^{\,2} / \left(\xi_c^{\,2} - 1\right)^2$$

$$\simeq \Gamma\ \eta^2 \left(\xi_c^{\,2} - 1\right) n_{0\xi} / \xi_c^{\,2}. \tag{B5}$$

The integral in (B4) can then be carried out,

$$I\ \nabla\cdot n_0 \nabla\tilde{\xi}\ \Phi_{0c\xi} = -\ \Gamma\ M\eta^2\left(\xi_c^{\,2} - 1\right)\ \tilde{\xi}_{\phi\phi}. \tag{B6}$$

Note that since $\eta \sim m^{-1/2}$ and $\partial\tilde{\xi}/\partial\phi \sim m$, the expression in (B6) has magnitude m, the same as (B2). The integral of the third term in (38) yields

$$I\ \nabla\cdot\tilde{\xi}n_{0\xi}\ \nabla\Phi_{0c} = \left(\xi_c^{\,2} - 1\right)\int_{\xi_c^-}^{\xi_c^+} d\xi$$

$$\times\ \left[\frac{\partial}{\partial\xi}\left(\xi^2 - 1\right)\tilde{\xi}n_{0\xi}\frac{\partial}{\partial\xi} + \frac{\partial}{\partial\eta}\left(1 - \eta^2\right)\tilde{\xi}n_{0\xi}\frac{\partial}{\partial\eta}\right.$$

$$\left. + \left(\frac{1}{\xi^2 - 1} + \frac{1}{1 - \eta^2}\right)\frac{\partial}{\partial\phi}\ \tilde{\xi}n_{0\xi}\frac{\partial}{\partial\phi}\right]\Phi_{0c}. \tag{B7}$$

The first and third terms in (B7) are zero, the first because $n_{0\xi} = 0$ on either size of the boundary and the third because $\partial\Phi_{0c}/\partial\phi = 0$ at the boundary. In the frame of the moving cloud, the polarization potential is zero inside the cloud and at the boundary while Φ_{0a} is independent of ϕ. The second term in (B7) is non-zero. However, since the second $\partial/\partial\eta$ in this term acts on an equilibrium quantity, and is therefore of order unity, we find

$$I\nabla\cdot\tilde{\xi}n_{0\xi}\nabla\Phi_{0c} \sim m^{1/2} \ll m.$$

This term is therefore small compared with the contributions from the first two terms of (38) and can be neglected. The fourth term in (38) yields,

$$I\left(\tilde{\xi}n_{0\xi}\right)_y = \int_{\xi_c^-}^{\xi_c^+} d\xi \left[\xi_y \frac{\partial}{\partial \xi} + \eta_y \frac{\partial}{\partial \eta} + \phi_y \frac{\partial}{\partial \phi}\right] \tilde{\xi}n_{0\xi} \tag{B8}$$

The first term in (B8) can be integrated by parts once to produce a term

$$\int_{\xi_c^-}^{\xi_c^+} d\xi \; \tilde{\xi}n_{0\xi} \frac{\partial}{\partial \xi} (\xi_y),$$

which is of order unity. The second term in (B8) is of order $m^{1/2}$ while the third is of order m. Thus, only the last term need be retained,

$$I\left(\tilde{\xi}n_{0\xi}\right)_y \simeq - M \cos\phi \; \tilde{\xi}_\phi, \tag{B9}$$

where $\phi_y \simeq \cos\phi$. The integral of the last term in (38), can be written as

$$I\left(\tilde{\xi}n_{0\xi}\right)_{zz} = \int_{\xi_c^-}^{\xi_c^+} d\xi \left(\eta_z{}^2 \frac{\partial^2}{\partial \eta^2} + \eta_{zz} \frac{\partial}{\partial \eta} + \xi_z{}^2 \frac{\partial^2}{\partial \xi^2}\right.$$

$$\left. + \xi_{zz} \frac{\partial}{\partial \xi} + 2\eta_z \xi_z \frac{\partial}{\partial \eta} \frac{\partial}{\partial \xi}\right) \tilde{\xi}n_{0\xi}. \tag{B10}$$

All of the operators $\partial/\partial\xi$ in the parenthesis of (B10) can be integrated by parts so that they act on equilibrium functions and are therefore of order one. Each $\partial/\partial\eta$ in the parenthesis is of order $m^{1/2}$. The dominant term in (B10) is therefore the first, which scales as $\partial^2/\partial\eta^2 \sim m$. Equation (B10) simplifies to

$$I\left(\tilde{\xi}n_{0\xi}\right)_{zz} = - M\left(\xi_c{}^2 - 1\right)\tilde{\xi}_{\eta\eta}, \tag{B11}$$

where η_z has been evaluated using (A11). Combining (B2), (B6), (B9) and (B11), we obtain the equation for the jump in the slope of $\tilde{\Phi}$ given in (41).

REFERENCES

1. A. Simon, Phys. Fluids, 6, 382 (1963).
2. F.C. Hoh, Phys. Fluids, 6, 1184 (1963).
3. L.M. Linson and J. Workman, J. Geophys. Res., 75, 3211 (1970).
4. J.N. Shiau and A. Simon, Phys. Rev. Lett., 29, 1664 (1972).
5. J.N. Shiau and A. Simon, J. Geophys. Res., 79, 1895 (1974).
6. S.H. Francis and F.W. Perkins, J. Geophys. Res., 80, 3111 (1975).
7. F.W. Perkins and J.H. Doles III, J. Geophys. Res., 80, 211 (1975).
8. S.R. Goldman, R.L. Baker, S.L. Ossakow, and A.J. Scannapieco, J. Geophys. Res., 81, 5097 (1976).
9. P.K. Chaturvedi and S.L. Ossakow, J. Geophys. Res., 84, 419 (1979).
10. M.J. Keskinen, S.L. Ossakow, and P.K. Chaturvedi, J. Geophys. Res., 85, 3485 (1980).
11. J.D. Huba, S.L. Ossakow, P. Satyanarayana, and P.N. Guzdar, J. Geophys. Res., 80, 425 (1983).
12. J.D. Huba and S.T. Zalesak, J. Geophys. Res., 88, 10263 (1983).
13. J.L. Sperling, J. Geophys. Res., 88, 4075 (1983).
14. J.L. Sperling, J. Geophys. Res., 89, 6793 (1984).
15. J.L. Sperling and A.J. Glassman, J. Geophys. Res., 90, 2819 (1985).
16. J.L. Sperling, J.F. Drake, S.T. Zalesak, and J.D. Huba, J. Geophys. Res., 89, 10913 (1984).
17. J.F. Drake, J.D. Huba, and S.T. Zalesak, J. Geophys. Res., 90, 5227 (1985).
18. J.F. Drake and J.D. Huba, J. Geophys. Res., 91, 10108 (1986).
19. J.F. Drake and J.D. Huba, Phys. Rev. Lett., 58, 278 (1987).
20. H.J. Volk and G. Haerendel, J. Geophys. Res., 76, 4541 (1971).

21. N.J. Zabusky, J.H. Doles III, and F.W. Perkins, J. Geophys. Res., 78, 711 (1973).

22. B.E. McDonald, M.J. Keskinen, S.L. Ossakow, and S.T. Zalesak, J. Geophys. Res., 85, 2143 (1980).

23. E.A. Overman, N.J. Zabusky, and S.L. Ossakow, Phys. Fluids, 26, 1139 (1983).

24. S.T. Zalesak, P.K. Chaturvedi, S.L. Ossakow, and J.A. Fedder, J. Geophys. Res., 90, 4299 (1985).

25. S.T. Zalesak, J.D. Huba, and J.F. Drake, EOS, 69, 422 (1988).

26. J.L. Sperling (private communication).

27. D.T. Farley, Jr., J. Geophys. Res., 64, 401 (1959).

28. C.W. Prettie (private communication).

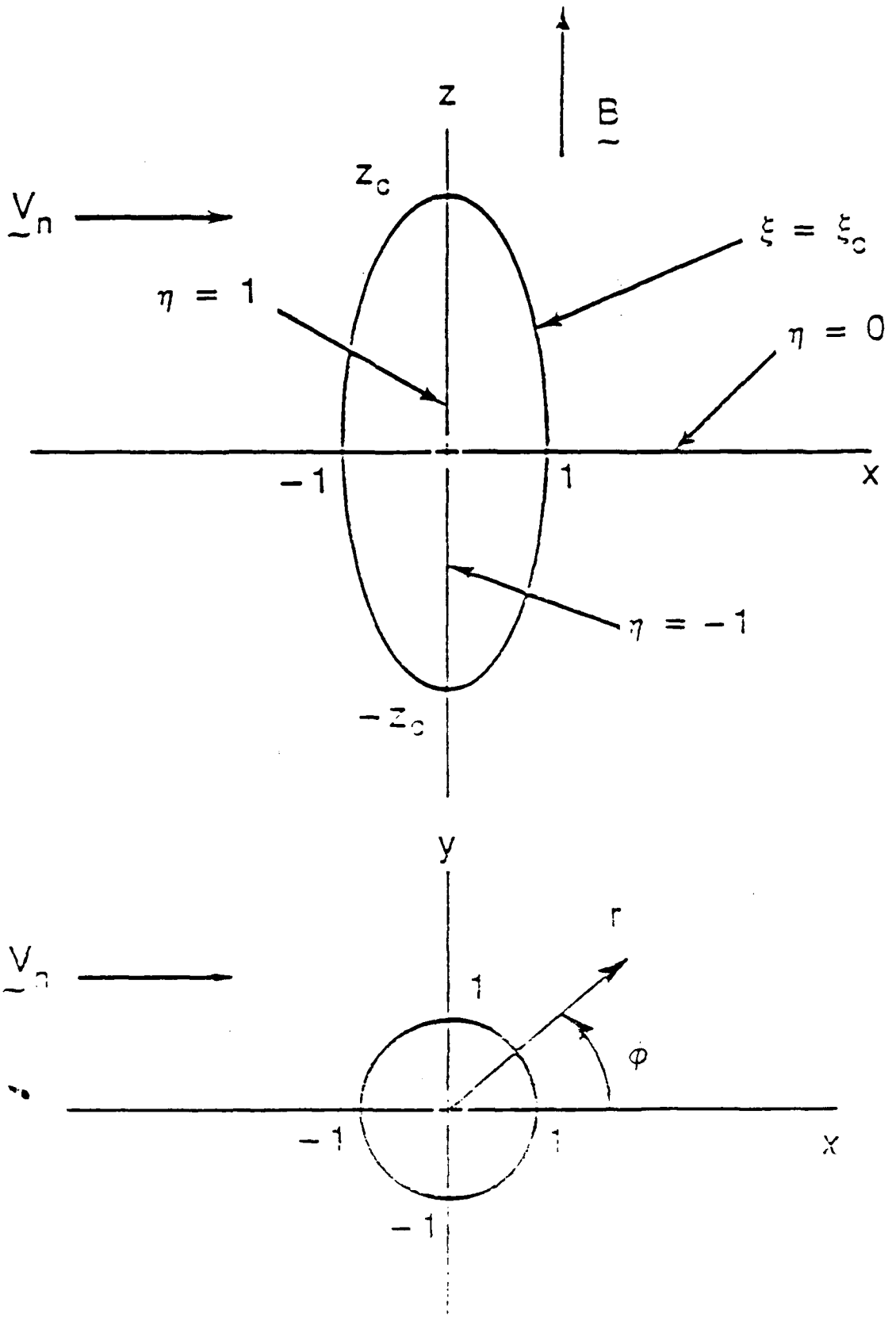

Fig. 1 — Plasma configuration and geometry. The cloud is an ellipsoidal waterbag (defined by $\zeta = \zeta_c$) of aspect ratio z_c (in normalized units). The cross-section is elliptical in the xz plane (a) and circular in the xy plane (b), which is transverse to $\underset{\sim}{B}$.

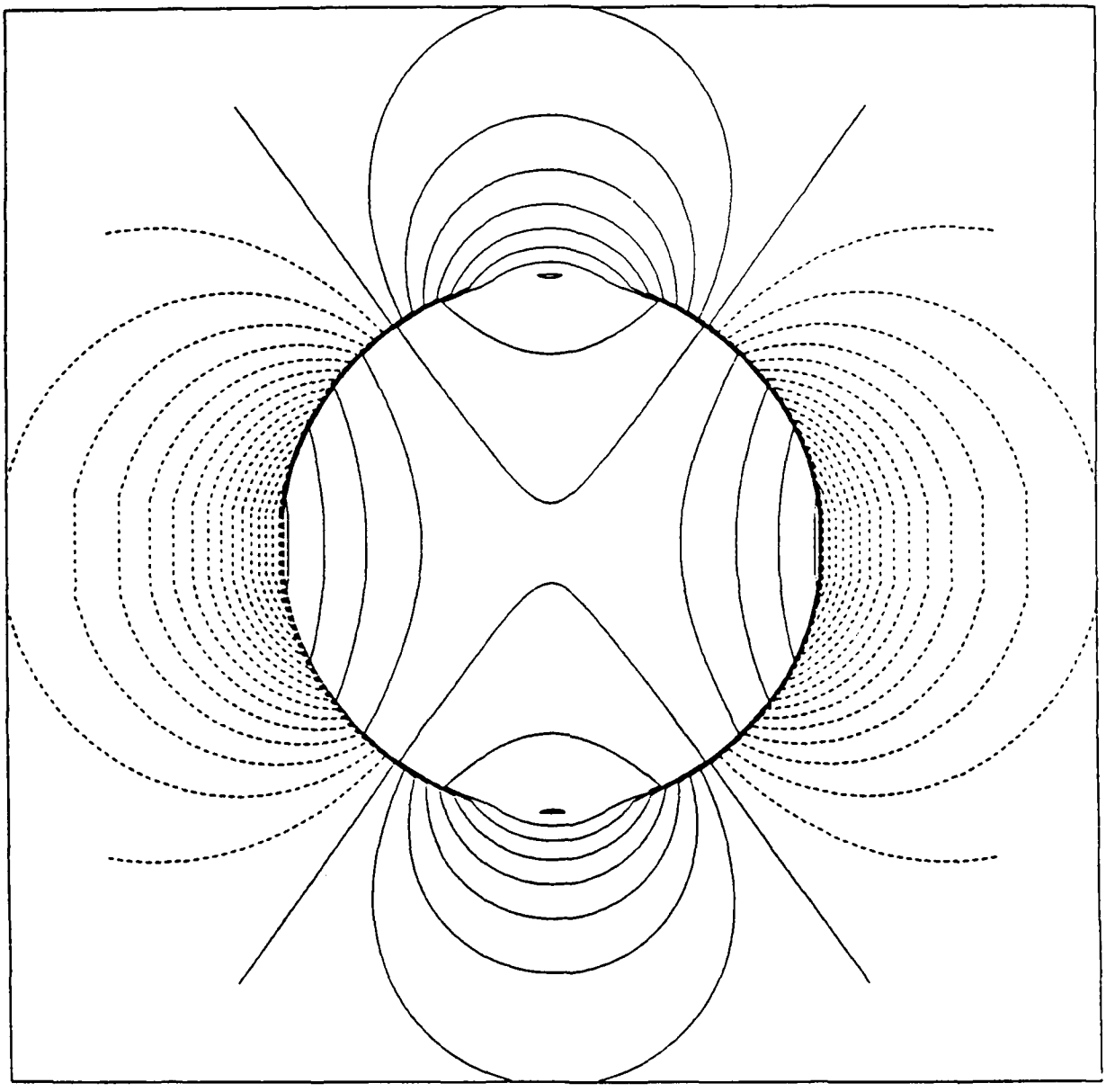

Fig. 2a — The contours of constant ambipolar potential Φ_{0a} and azimuthal rotation rate $\omega_{0a} = (\partial \Phi_{0a}/\partial r)/r$ in (a) and (b), respectively, for $z_c = 1.0$, $M = 5.0$, and $\Gamma_c = 1.0$. The magnetic field is upward in (a) and (b) and in corresponding plots in Figs. 3 and 4. Contours are equally spaced with solid (dashed) lines representing positive (negative) values. The rotation rate ω_{0a} versus ν at the midplane ($z = 0$) is shown in (c). The plasma cloud ($r < 1$) rotates as a solid body.

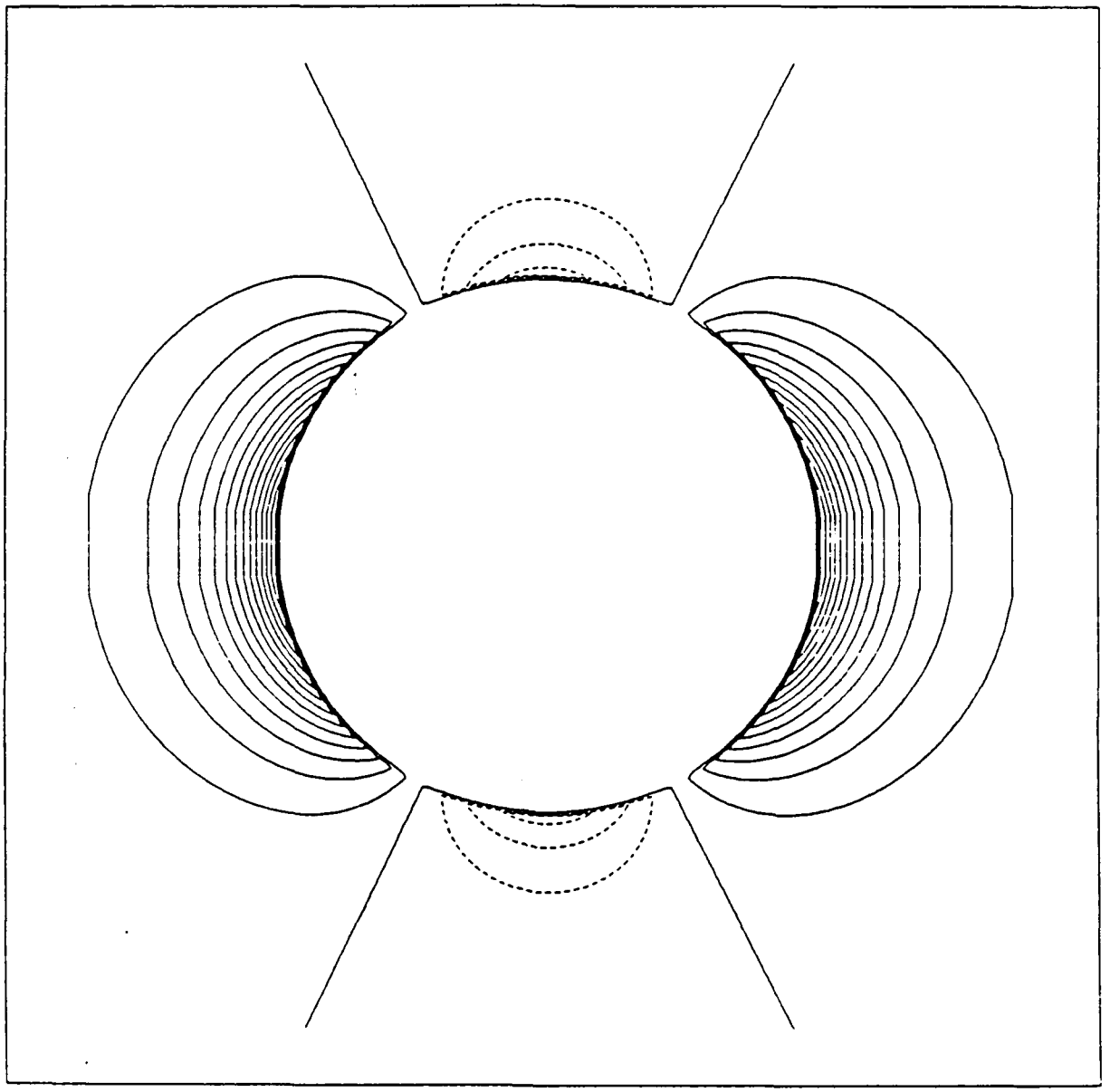

Fig. 2b — The contours of constant ambipolar potential Φ_{0a} and azimuthal rotation rate $\omega_{0a} = (\partial \Phi_{0a}/\partial r)/r$ in (a) and (b), respectively, for $z_c = 1.0$, $M = 5.0$, and $\Gamma_c = 1.0$. The magnetic field is upward in (a) and (b) and in corresponding plots in Figs. 3 and 4. Contours are equally spaced with solid (dashed) lines representing positive (negative) values. The rotation rate ω_{0a} versus ν at the midplane ($z = 0$) is shown in (c). The plasma cloud ($r < 1$) rotates as a solid body.

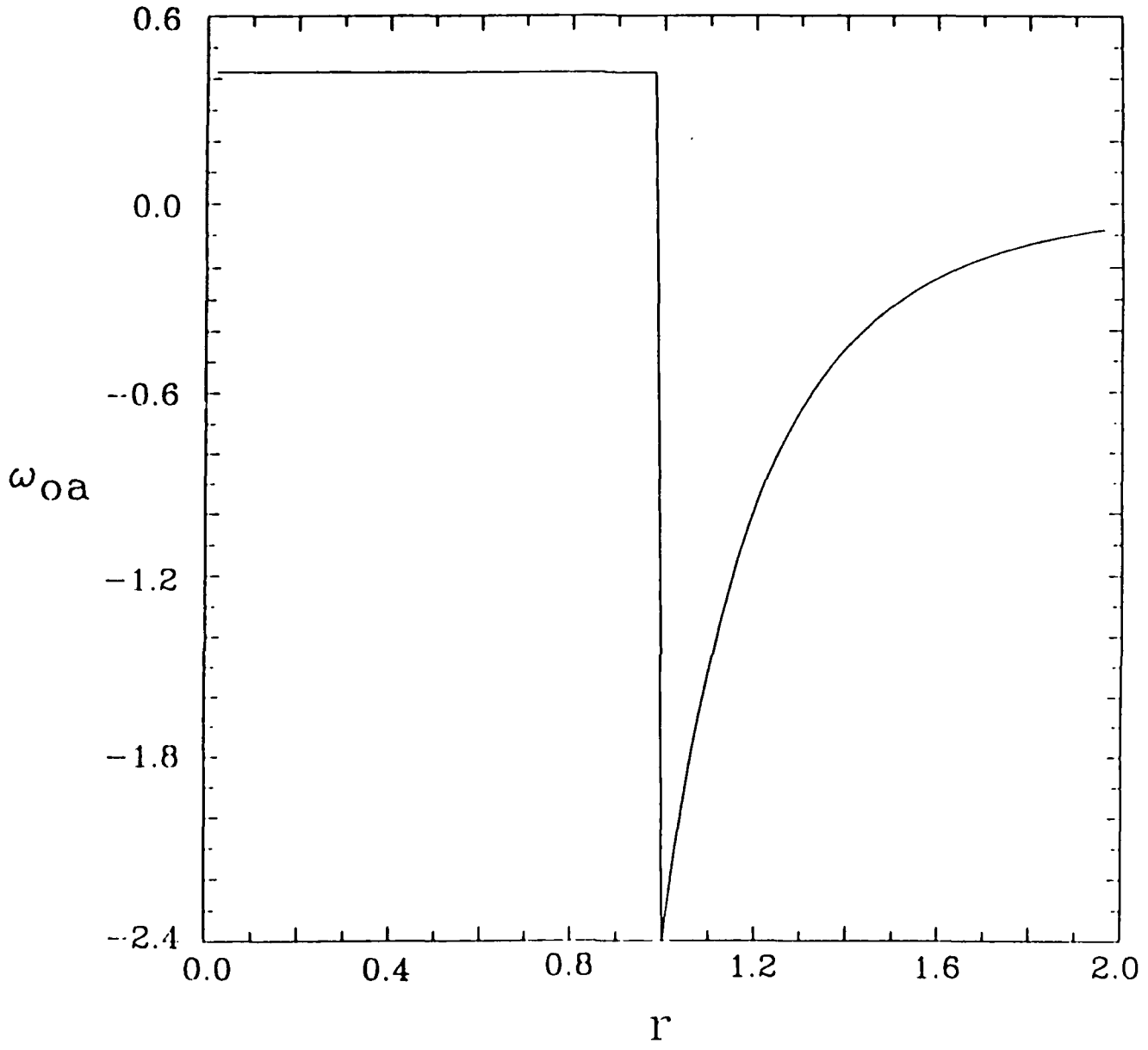

Fig. 2c — The contours of constant ambipolar potential Φ_{0a} and azimuthal rotation rate $\omega_{0a} = (\partial \Phi_{0a}/\partial r)/r$ in (a) and (b), respectively, for $z_c = 1.0$, $M = 5.0$, and $\Gamma_c = 1.0$. The magnetic field is upward in (a) and (b) and in corresponding plots in Figs. 3 and 4. Contours are equally spaced with solid (dashed) lines representing positive (negative) values. The rotation rate ω_{0a} versus ν at the midplane ($z = 0$) is shown in (c). The plasma cloud ($r < 1$) rotates as a solid body.

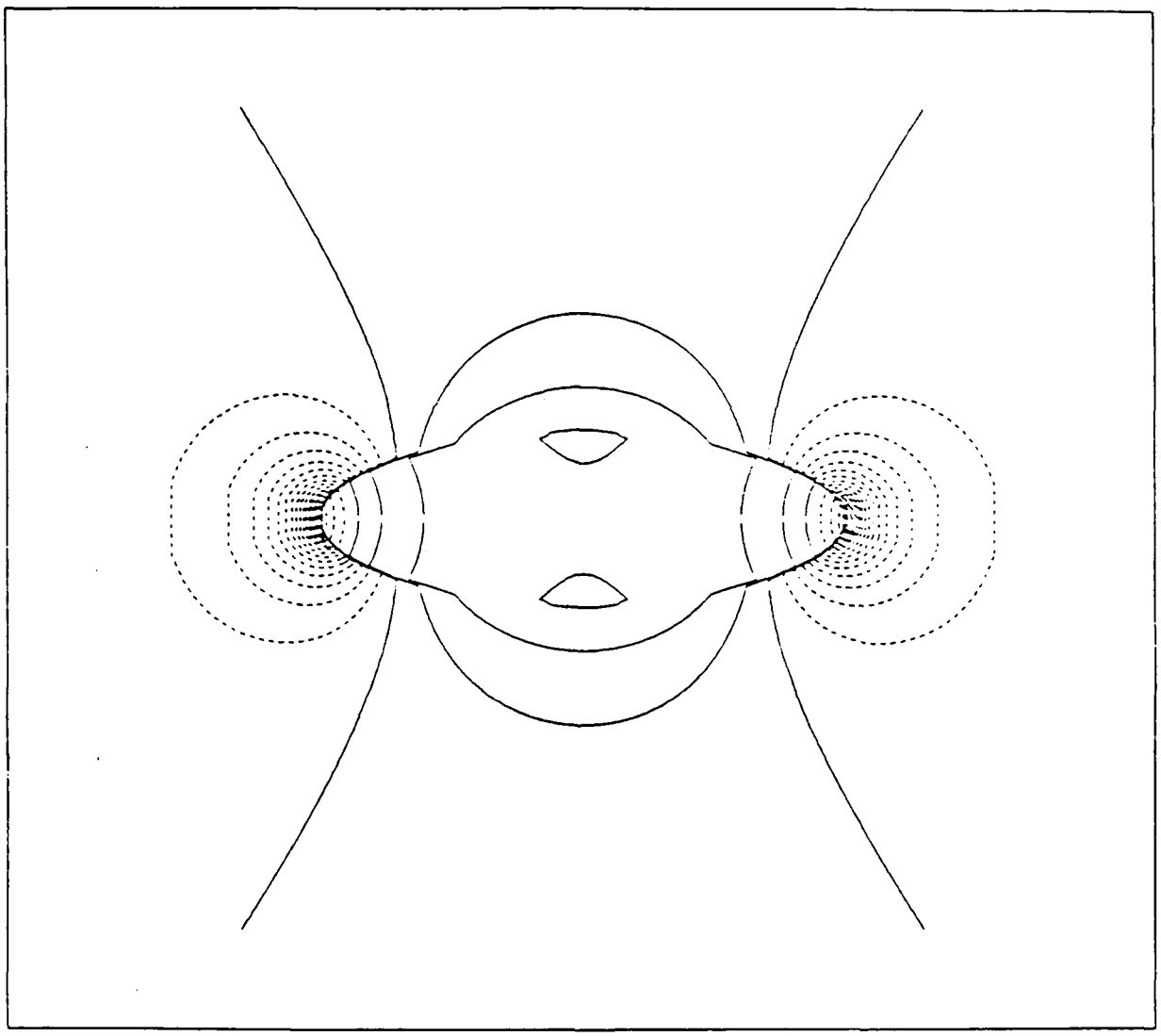

Fig. 3a — Plots similar to those shown in Fig. 2 but with $z_c = 3.0$. The aximuthal flows are rather strongly localized around the top and bottom of the cloud.

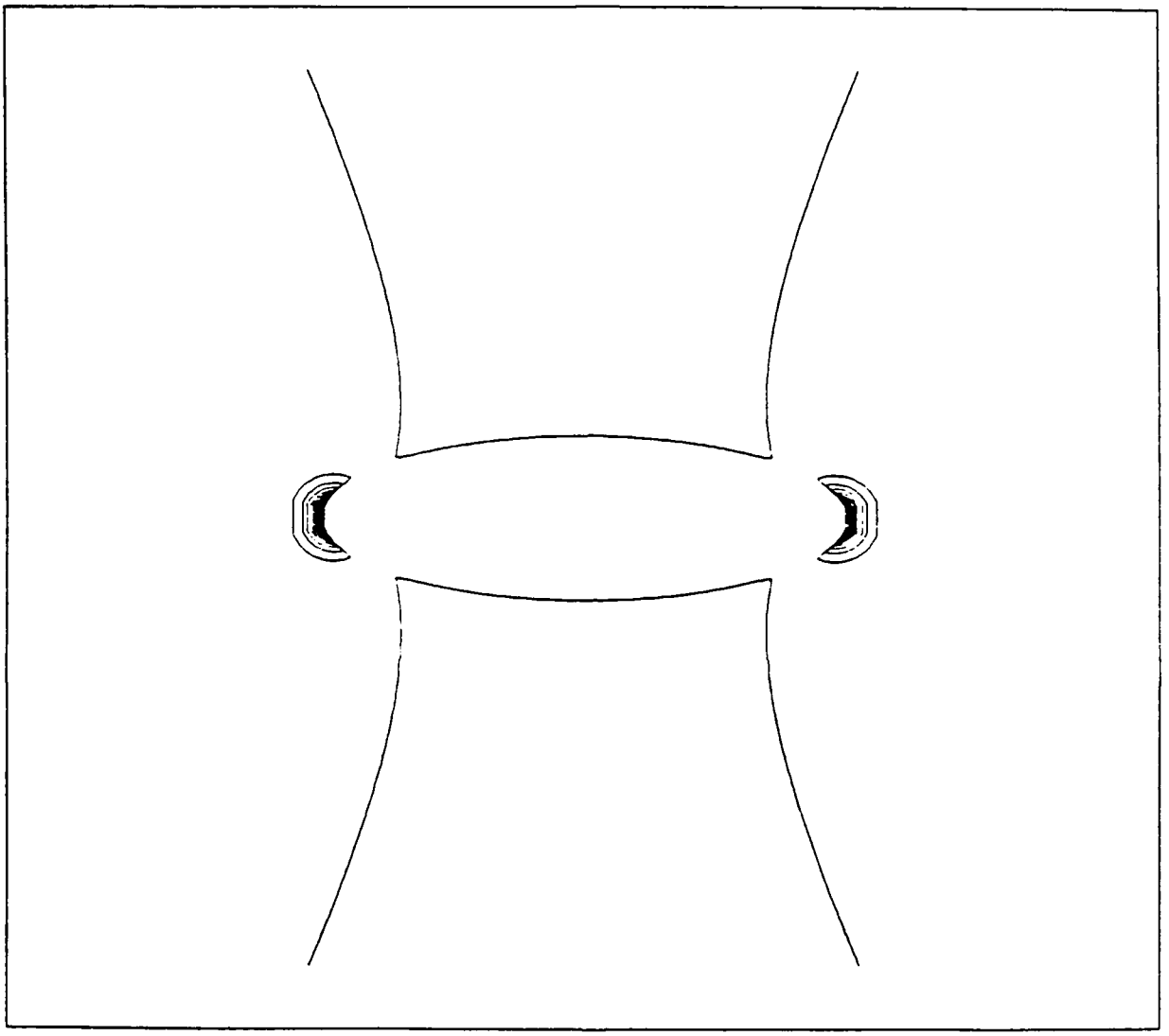

Fig. 3b — Plots similar to those shown in Fig. 2 but with $z_c = 3.0$. The aximuthal flows are rather strongly localized around the top and bottom of the cloud.

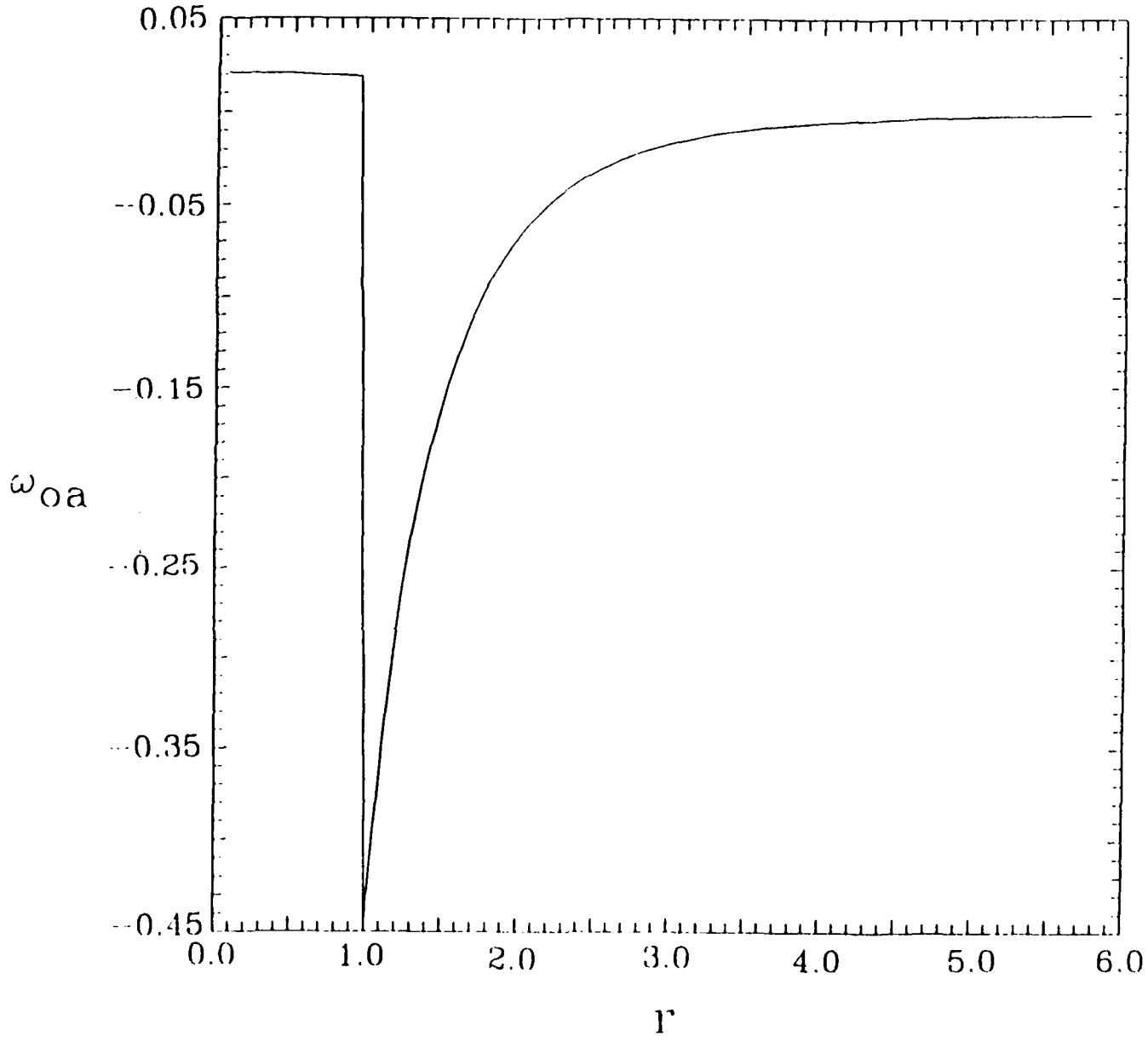

Fig. 3c — Plots similar to those shown in Fig. 2 but with $z_c = 3.0$. The aximuthal flows are rather strongly localized around the top and bottom of the cloud.

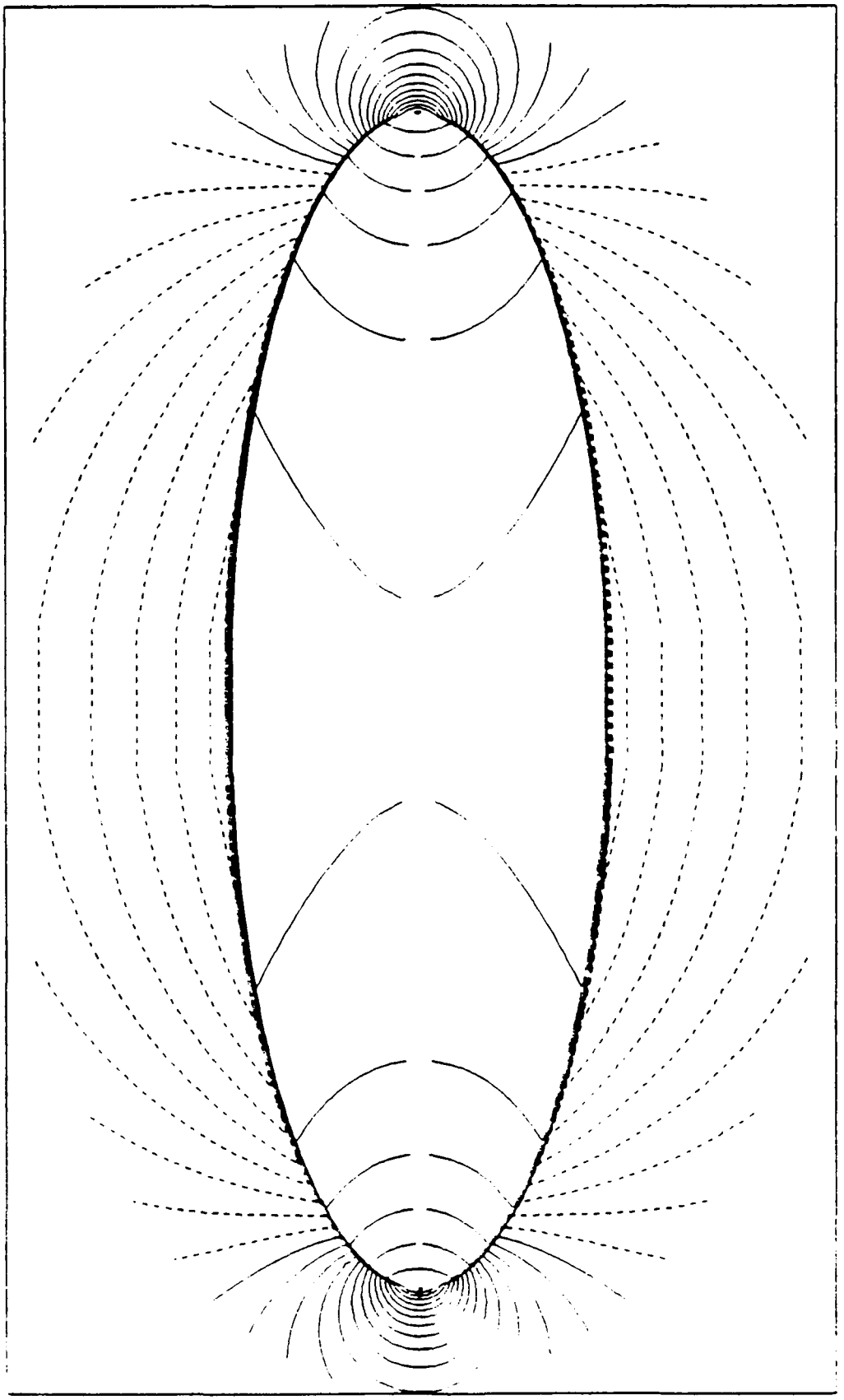

Fig. 4a — Plots similar to those shown in Figs. 2 and 3 but with $z_c = 1/3$. The rotation rate inside the cloud is strongly non-uniform.

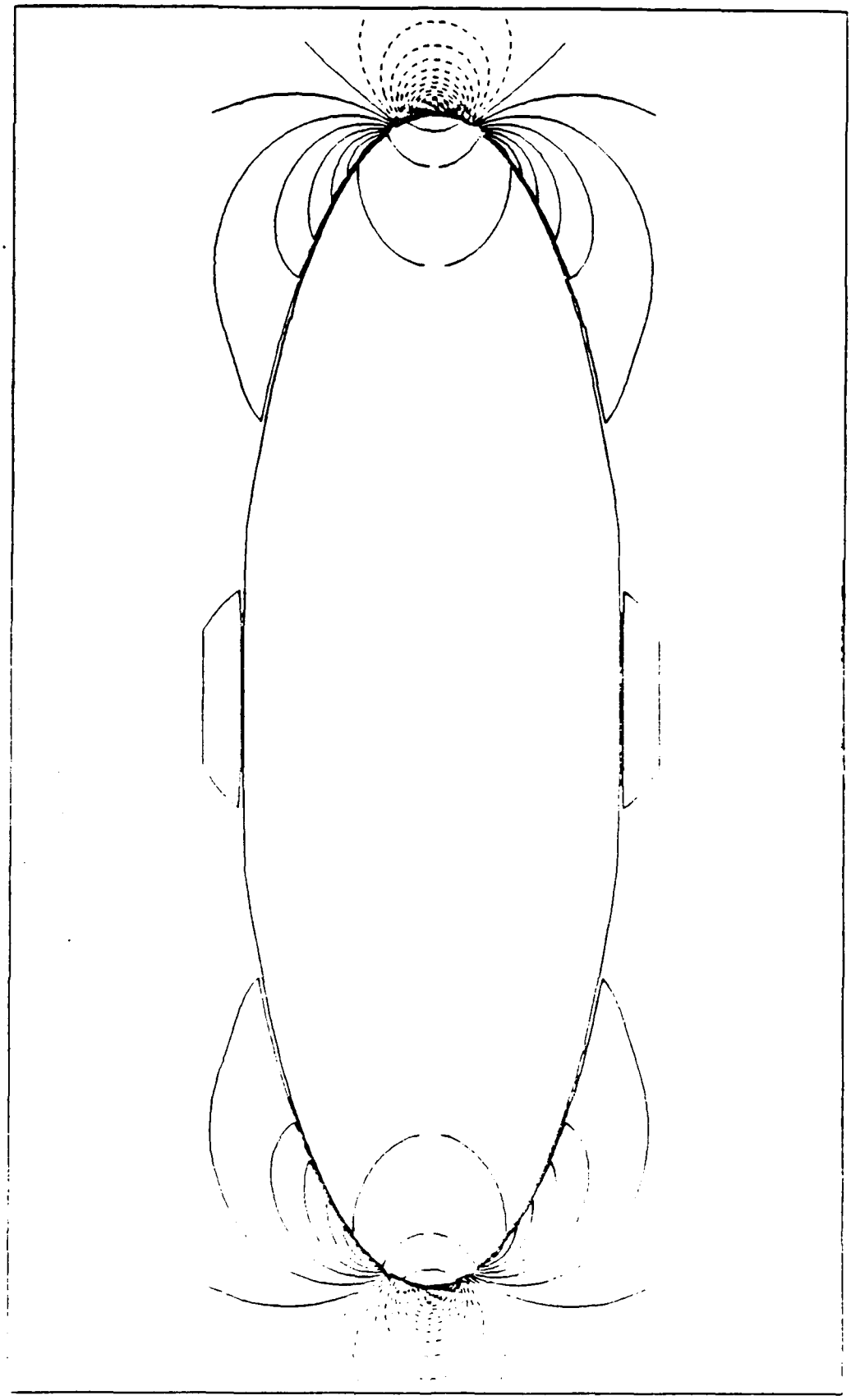

Fig. 4b — Plots similar to those shown in Figs. 2 and 3 but with $z_c = 1/3$. The rotation rate inside the cloud is strongly non-uniform.

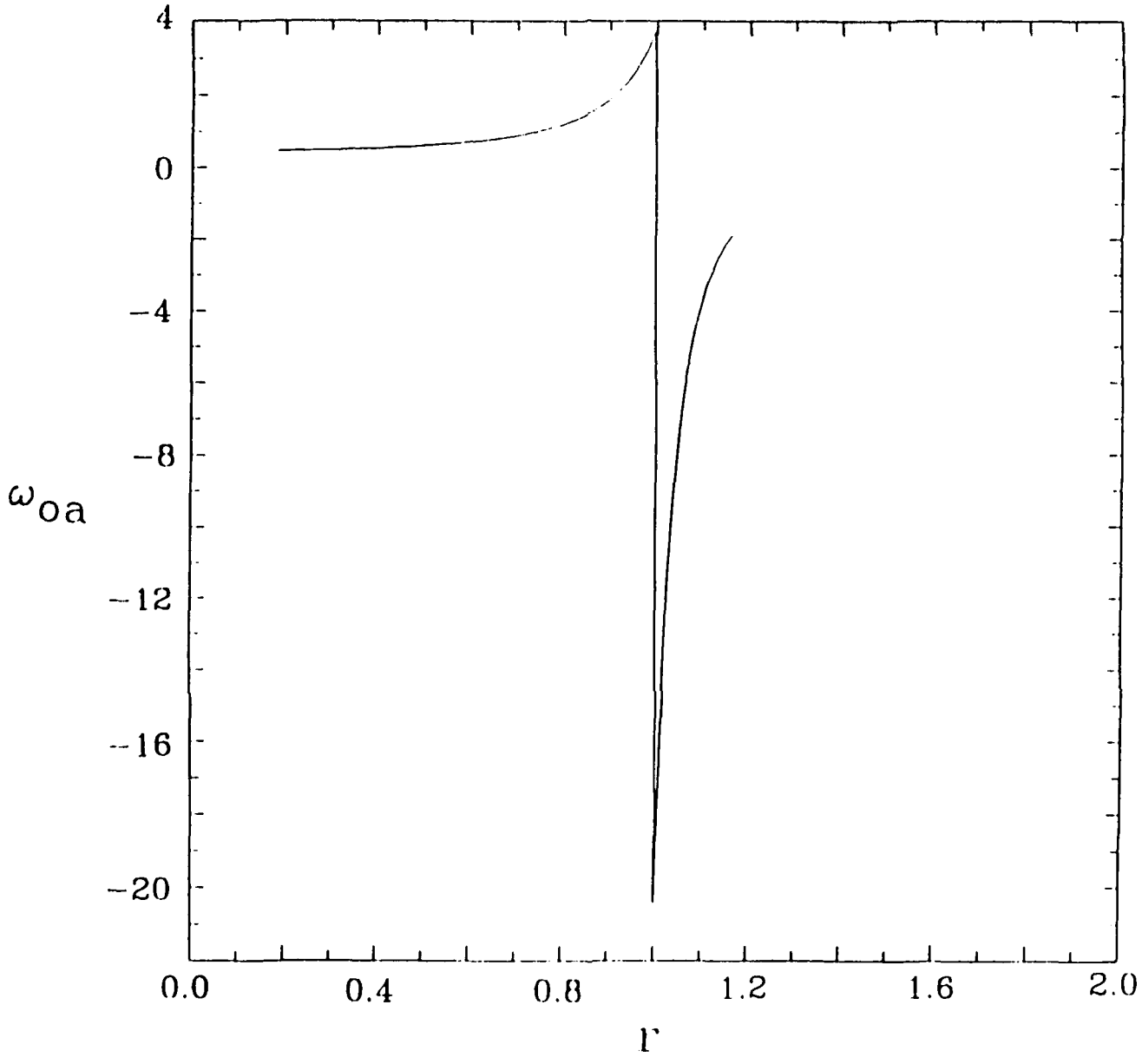

Fig. 4c — Plots similar to those shown in Figs. 2 and 3 but with $z_c = 1/3$. The rotation rate inside the cloud is strongly non-uniform.

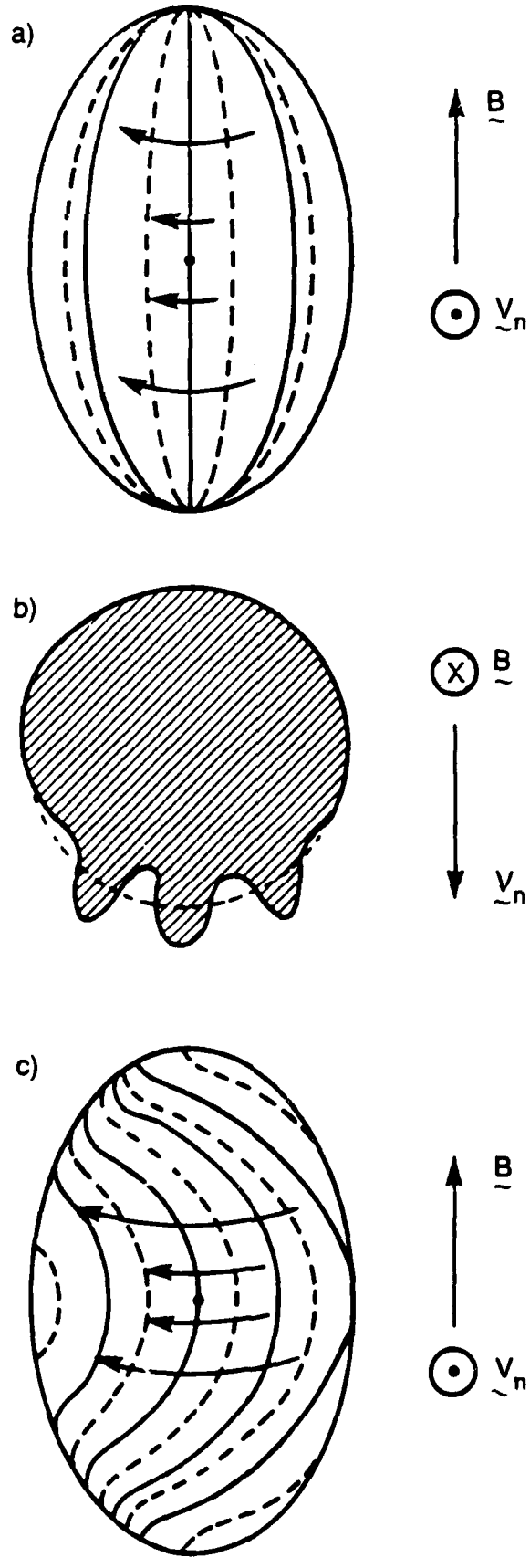

Fig. 5 — Schematic of shear stabilization. View of the cloud from the backside (a) and bottom (b) illustrate the growth of flute-like striations. Solid (dashed) lines in (a) indicate plasma motion outward (inward). Aximuthal arrows in (a) indicate the propagation of the local perturbation leading to non-flute characters in (c).

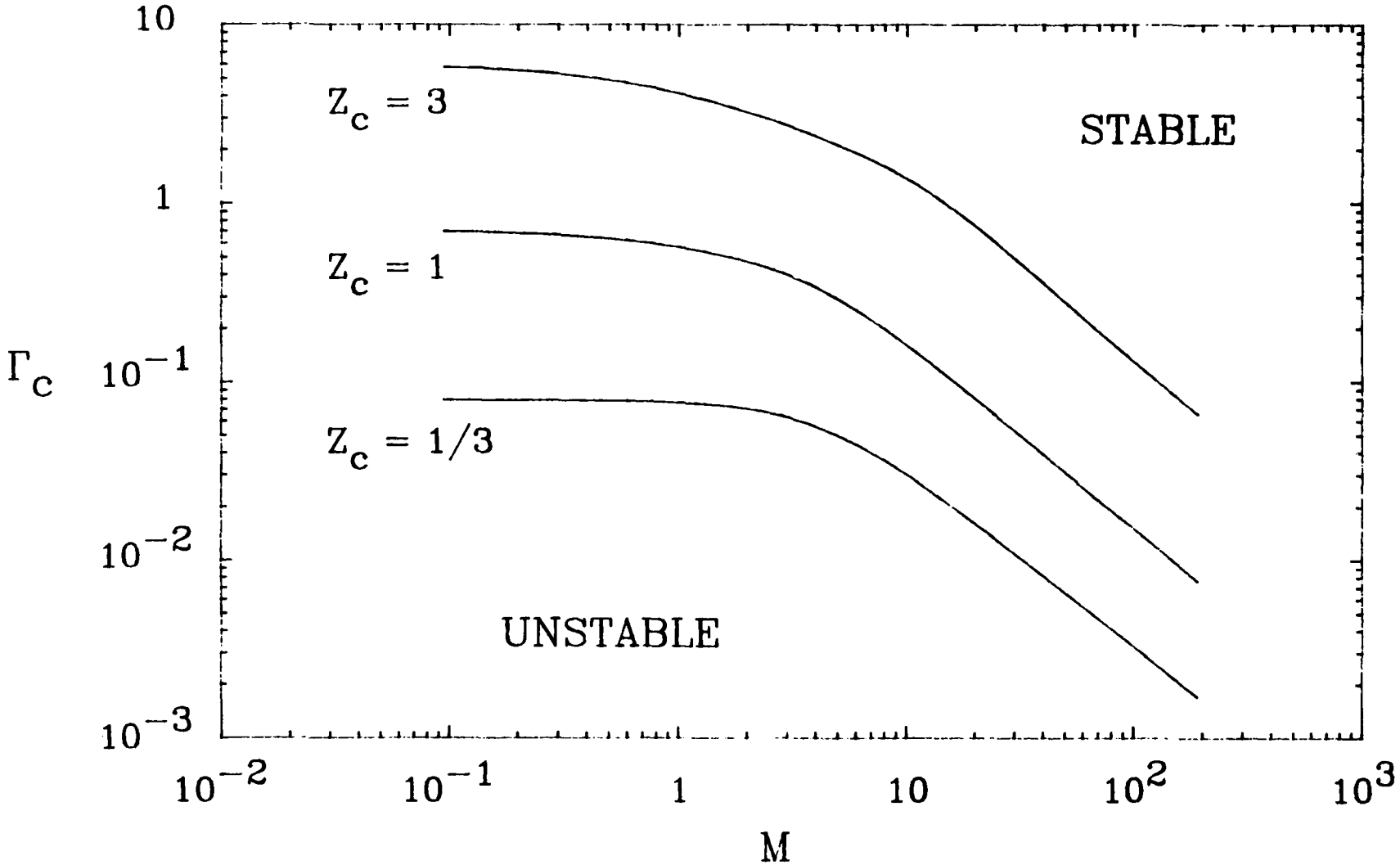

Fig. 6 — Critical value of Γ for stability versus M for $z_c = 1/3$, 1 and 3. The cloud is stable for $\Gamma > \Gamma_c$.

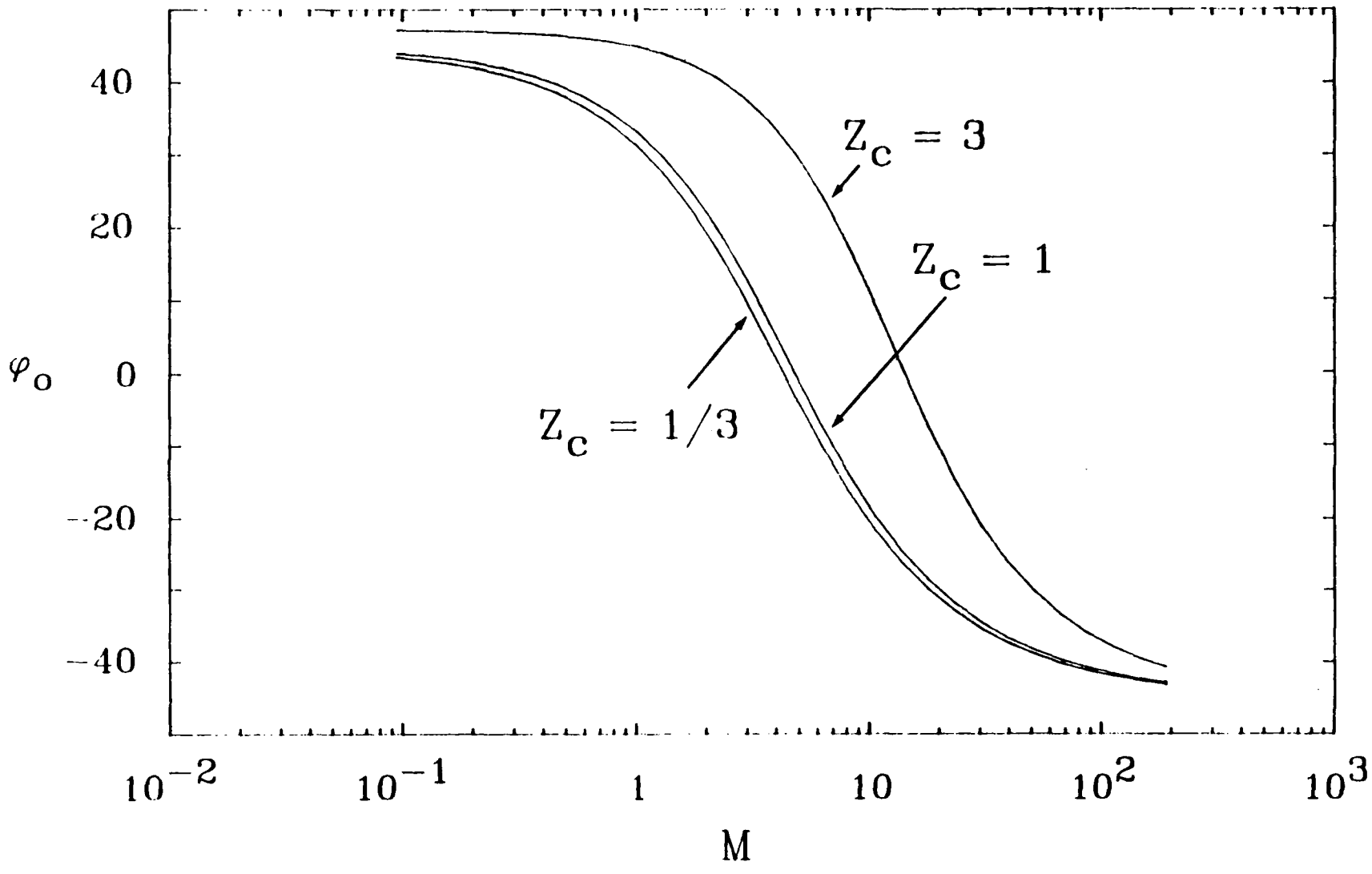

Fig. 7 — Azimuthal location of non-propagating solution at marginal stability ($\Gamma = \Gamma_c$).

DISTRIBUTION LIST
(Unclassified Only)

DEPARTMENT OF DEFENSE

ASSISTANT SECRETARY OF DEFENSE
COMM, CMD, CONT 7 INTELL
WASHINGTON, DC 20301

DIRECTOR
COMMAND CONTROL TECHNICAL CENTER
PENTAGON RM BE 685
WASHINGTON, DC 20301
01CY ATTN C-650
01CY ATTN C-312/R. MASON

DIRECTOR
DEFENSE ADVANCED RSCH PROJ AGENCY
ARCHITECT BUILDING
1400 WILSON BLVD.
ARLINGTON, VA 22209
01CY ATTN NUCLEAR MONITORING RESEARCH
01CY ATTN STRATEGIC TECH OFFICE

DEFENSE COMMUNICATION ENGINEER CENTER
1860 WIEHLE AVENUE
RESTON, VA 22090
01CY ATTN CODE R410
01CY ATTN CODE R812

DIRECTOR
DEFENSE NUCLEAR AGENCY
WASHINGTON, DC 20305
01CY ATTN STVL
04CY ATTN TITL
01CY ATTN DDST
03CY ATTN RAAE

COMMANDER
FIELD COMMAND
DEFENSE NUCLEAR AGENCY
KIRTLAND AFB, NM 87115
01CY ATTN FCPR

DEFENSE NUCLEAR AGENCY
SAO/DNA
BUILDING 20676
KIRTLAND AFB, NM 87115
01CY ATTN D. THORNBURG

DIRECTOR
INTERSERVICE NUCLEAR WEAPONS SCHOOL
KIRTLAND AFB, NM 87115
01CY ATTN DOCUMENT CONTROL

JOINT PROGRAM MANAGEMENT OFFICE
WASHINGTON, DC 20330
01CY ATTN J-3 WWMCCS EVALUATION OFFICE

DIRECTOR
JOINT STRAT TGT PLANNING STAFF
OFFUTT AFB
OMAHA, NB 68113
01CY ATTN JSTPS/JLKS
01CY ATTN JPST/G. GOETZ

CHIEF
LIVERMORE DIVISION FLD COMMAND DNA
DEPARTMENT OF DEFENSE
LAWRENCE LIVERMORE LABORATORY
P.O. BOX 808
LIVERMORE, CA 94550
01CY ATTN FCPRL

COMMANDANT
NATO SCHOOL (SHAPE)
APO NEW YORK 09172
01CY ATTN U.S. DOCUMENTS OFFICER

UNDER SECY OF DEFENSE FOR
RESEARCH AND ENGINEERING
DEPARTMENT OF DEFENSE
WASHINGTON, DC 20301
01CY ATTN STRATETIC & SPACE SYSTEMS (OS)

COMMANDER/DIRECTOR
ATMOSPHERIC SCIENCES LABORATORY
U.S. ARMY ELECTRONICS COMMAND
WHITE SANDS MISSILE RANGE, NM 88002
01CY ATTN DELAS-EO/F. NILES

DIRECTOR
BMD ADVANCED TECH CENTER
HUNTSVILLE OFFICE
P.O. BOX 1500
HUNTSVILLE, AL 35807
01CY ATTN ATC-T/MELVIN CAPPS
01CY ATTN ATC-O/W. DAVIES
01CY ATTN ATC-R/DON RUSS

PROGRAM MANAGER
BMD PROGRAM OFFICE
5001 EISENHOWER AVENUE
ALEXANDRIA, VA 22333
01CY ATTN DACS-BMT/J. SHEA

COMMANDER
U.S. ARMY COMM-ELEC ENGINEERING
INSTALLATION AGENCY
FT. HUACHUCA, AZ 85613
01CY ATTN CCC-EMEO/GEORGE LANE

COMMANDER
U.S. ARMY FOREIGN SCIENCE & TECH CTR
220 7TH STREET, N.E.
CHARLOTTESVILLE, VA 22901
01CY ATTN DRXST-SD

COMMANDER
U.S. ARMY MATERIAL DEV & READINESS
COMMAND
5001 EISENHOWER AVENUE
ALEXANDRIA, VA 22333
01CY ATTN DRCLDC/J.A. BENDER

COMMANDER
U.S. ARMY NUCLEAR AND CHEMICAL AGENCY
7500 BACKLICK ROAD
BLDG 2073
SPRINGFIELD, VA 22150
01CY ATTN LIBRARY

DIRECTOR
U.S. ARMY BALLISTIC RESEARCH
LABORATORY
ABERDEEN PROVING GROUND, MD 21005
01CY ATTN TECH LIBRARY/
EDWARD BAICY

COMMANDER
U.S. ARMY SATCOM AGENCY
FT. MONMOUTH, NJ 07703
01CY ATTN DOCUMENT CONTROL

COMMANDER
U.S. ARMY MISSILE INTELLIGENCE AGENCY
REDSTONE ARSENAL, AL 35809
01CY ATTN JIM GAMBLE

DIRECTOR
U.S. ARMY TRADOC SYSTEMS ANALYSIS
ACTIVITY
WHITE SANDS MISSILE RANGE, NM 88002
01CY ATTN ATAA-SA
01CY ATTN TCC/F. PAYAN, JR.
01CY ATTN ATTA-TAC/LTC J. HESSE

COMMANDER
NAVAL ELECTRONIC SYSTEMS COMMAND
WASHINGTON, DC 20360
01CY ATTN NAVALEX 034/T. HUGHES
01CY ATTN PME 117
01CY ATTN PME 117-T
01CY ATTN CODE 5011

COMMANDING OFFICER
NAVAL INTELLIGENCE SUPPORT CENTER
4301 SUITLAND ROAD, BLDG. 5
WASHINGTON, DC 20390
01CY ATTN MR. DUBBIN/STIC 12
01CY ATTN NISC-50
01CY ATTN CODE 5404/J. GALET

COMMANDER
NAVAL OCEAN SYSTEMS CENTER
SAN DIEGO, CA 92152
01CY ATTN J. FERGUSON

NAVAL RESEARCH LABORATORY
WASHINGTON, DC 20375-5000
26CY ATTN CODE 4700/S. OSSAKOW
50CY ATTN CODE 4780/J. HUBA
01CY ATTN CODE 4701
01CY ATTN CODE 7500
01CY ATTN CODE 7550
01CY ATTN CODE 7580
01CY ATTN CODE 7551
01CY ATTN CODE 7555
01CY ATTN CODE 4730/E. MCLEAN
01CY ATTN CODE 4752
01CY ATTN CODE 4730/B. RIPIN
20CY ATTN CODE 2628
01CY ATTN CODE 1004/P. MANGE
01CY ATTN CODE 8344/M. KAPLAN

COMMANDER
NAVAL SPACE SURVEILLANCE SYSTEM
DAHLGREN, VA 22448
01CY ATTN CAPT. J.H. BURTON

OFFICER-IN-CHARGE
NAVAL SURFACE WEAPONS CENTER
WHITE OAK, SILVER SPRING, MD 20910
01CY ATTN CODE F31

DIRECTOR
STRATEGIC SYSTEMS PROJECT OFFICE
DEPARTMENT OF THE NAVY
WASHINGTON, DC 20376
01CY ATTN NSP-2141
01CY ATTN NSSP-2722/
FRED WIMBERLY

COMMANDER
NAVAL SURFACE WEAPONS CENTER
DAHLGREN LABORATORY
DAHLGREN, VA 22448
01CY ATTN CODE DF-14/R. BUTLER

OFFICER OF NAVAL RESEARCH
ARLINGTON, VA 22217
01CY ATTN CODE 465
01CY ATTN CODE 461
01CY ATTN CODE 402
01CY ATTN CODE 420
01CY ATTN CODE 421

COMMANDER
AEROSPACE DEFENSE COMMAND/XPD
DEPARTMENT OF THE AIR FORCE
ENT AFB, CO 80912
01CY ATTN XPDQQ
01CY ATTN XP

AIR FORCE GEOPHYSICS LABORATORY
HANSCOM AFB, MA 01731
01CY ATTN OPR/HAROLD GARDNER
01CY ATTN LKB/
KENNETH S.W. CHAMPION
01CY ATTN OPR/ALVA T. STAIR
01CY ATTN PHD/JURGEN BUCHAU
01CY ATTN PHD/JOHN P. MULLEN

AF WEAPONS LABORATORY
KIRTLAND AFB, NM 87117
01CY ATTN SUL
01CY ATTN CA/ARTHUR H. GUENTHER

AFTAC
PATRICK AFB, FL 32925
01CY ATTN TN

WRIGHT AERONAUTICAL LABORATORIES
WRIGHT-PATTERSON AFB, OH 45433-6543
01CY ATTN AAAI/WADE HUNT
01CY ATTN AAAI/ALLEN JOHNSON

DEPUTY CHIEF OF STAFF
RESEARCH, DEVELOPMENT, AND ACQ
DEPARTMENT OF THE AIR FORCE
WASHINGTON, DC 20330
01CY ATTN AFRDQ

HEADQUARTERS
ELECTRONIC SYSTEMS DIVISION
DEPARTMENT OF THE AIR FORCE
HANSCOM AFB, MA 01731-5000
01CY ATTN J. DEAS
ESD/SCD-4

COMMANDER
FOREIGN TECHNOLOGY DIVISION, AFSC
WRIGHT-PATTERSON AFB, OH 45433
01CY ATTN NICD/LIBRARY
01CY ATTN ETDP/B. BALLARD

COMMANDER
ROME AIR DEVELOPMENT CENTER, AFSC
GRIFFIN AFB, NY 13441
01CY ATTN DOC LIBRARY/TSLD
01CY ATTN OCSE/V. COYNE

STRATEGIC AIR COMMAND/XPFS
OFFUTT AFB, NB 68113
01CY ATTN XPFS

SAMSO/MN
NORTON AFB, CA 02409
(MINUTEMAN)
01CY ATTN MNNL

COMMANDER
ROME AIR DEVELOPMENT CENTER, AFSC
HANSCOM AFB, MA 01731
01CY ATTN EEP/A. LORENTZEN

DEPARTMENT OF ENERGY
LIBRARY, ROOM G-042
WASHINGTON, DC 20545
01CY ATTN DOC CON FOR
A. LABOWITZ

DEPARTMENT OF ENERGY
ALBUQUERQUE OPERATIONS OFFICE
P.O. BOX 5400
ALBUQUERQUE, NM 87115
01CY ATTN DOC CON FOR
D. SHERWOOD

EG&G, INC.
LOS ALAMOS DIVISION
P.O. BOX 809
LOS ALAMOS, NM 85544
01CY ATTN DOC CON FOR
J. BREEDLOVE

UNIVERSITY OF CALIFORNIA
LAWRENCE LIVERMORE LABORATORY
P.O. BOX 808
LIVERMORE, CA 94550
01CY ATTN DOC CON FOR
TECH INFO DEPT
01CY ATTN DOC CON FOR
L-389/R. OTT
01CY ATTN DOC CON FOR
L-31/R. HAGER

LOS ALAMOS NATIONAL LABORATORY
P.O. BOX 1663
LOS ALAMOS, NM 87545
01CY ATTN J. WOLCOTT
01CY ATTN R.F. TASCHEK
01CY ATTN E. JONES
01CY ATTN J. MALIK
01CY ATTN R. JEFFRIES
01CY ATTN J. ZINN
01CY ATTN D. WESTERVELT
01CY ATTN D. SAPPENFIELD

LOS ALAMOS NATIONAL LABORATORY
MS D438
LOS ALAMOS, NM 87545
01CY ATTN S.P. GARY
01CY ATTN J. BOROVSKY

SANDIA LABORATORIES
P.O. BOX 5800
ALBUQUERQUE, NM 87115
01CY ATTN W. BROWN
01CY ATTN A. THORNBROUGH
01CY ATTN T. WRIGHT
01CY ATTN D. DAHLGREN
01CY ATTN 3141
01CY ATTN SPACE PROJ DIV

SANDIA LABORATORIES
LIVERMORE LABORATORY
P.O. BOX 969
LIVERMORE, CA 94550
01CY ATTN B. MURPHEY
01CY ATTN T. COOK

OFFICE OF MILITARY APPLICATION
DEPARTMENT OF ENERGY
WASHINGTON, DC 20545
01CY ATTN DR. YO SONG

NATL. OCEANIC & ATMOSPHERIC
ADMINISTRATION
ENVIRONMENTAL RESEARCH LABS
DEPARTMENT OF COMMERCE
BOULDER, CO 80302
01CY ATTN R. GRUBB

DEPARTMENT OF DEFENSE CONTRACTORS

AEROSPACE CORPORATION
P.O. BOX 92957
LOS ANGELES, CA 90009
01CY ATTN I. GARFUNKEL
01CY ATTN T. SALMI
01CY ATTN V. JOSEPHSON
01CY ATTN S. BOWER
01CY ATTN D. OLSEN

ANALYTICAL SYSTEMS ENGINEERING CORP
5 OLD CONCORD ROAD
BURLINGTON, MA 01803
01CY ATTN RADIO SCIENCES

AUSTIN RESEARCH ASSOCIATION, INC.
1901 RUTLAND DRIVE
AUSTIN, TX 78758
01CY ATTN L. SLOAN
01CY ATTN R. THOMPSON

BERKELEY RESEARCH ASSOCIATES, INC.
P.O. BOX 983
BERKELEY, CA 94701
01CY ATTN J. WORKMAN
01CY ATTN C. PRETTIE
01CY ATTN S. BRECHT

BOEING COMPANY, THE
P.O. BOX 3707
SEATTLE, WA 98124
01CY ATTN G. KEISTER
01CY ATTN D. MURRAY
01CY ATTN G. HALL
01CY ATTN J. KENNEY

CHARLES STARK DRAPER LABORATORY
555 TECHNOLOGY SQUARE
CAMBRIDGE, MA 92139
01CY ATTN D.B. COX
01CY ATTN J.P. GILMORE

COMSAT LABORATORIES
22300 COMSAT DRIVE
CLARKSBURG, MD 20871
01CY ATTN G. HYDE

CORNELL UNIVERSITY
DEPT OF ELECTRICAL ENGINEERING
ITHACA, NY 14850
01CY ATTN D.T. FARLEY, JR.

ELECTROSPACE SYSTEMS, INC.
BOX 1359
RICHARDSON, TX 75080
01CY ATTN H. LOGSTON
01CY ATTN SECURITY/
(PAUL PHILLIPS)

EOS TECHNOLOGIES, INC.
606 WILSHIRE BLVD.
SANTA MONICA, CA 90401
01CY ATTN C.G. GABBARD
01CY ATTN R. LELEVIER

GEOPHYSICAL INSTITUTE
UNIVERSITY OF ALASKA
FAIRBANKS, AK 99701
01CY ATTN SECURITY OFFICER
01CY ATTN T.N. DAVIS
01CY ATTN NEAL BROWN

GTE SYLVANIA, INC.
ELECTRONICS SYSTEMS GRP-
EASTERN DIVISION
77 A STREET
NEEDHAM, MA 02194
01CY ATTN DICK STEINHOF

HSS, INC.
2 ALFRED CIRCLE
BEDFORD, MA 01730
01CY ATTN DONALD HANSEN

ILLINOIS, UNIVERSITY OF
107 COBLE HALL
150 DAVENPORT HOUSE
CHAMPAIGN, IL 61820
01CY ATTN DAN MCCLELLAND
01CY ATTN K. YEH

INSTITUTE FOR DEFENSE ANALYSIS
1801 NO. BEAUREGARD STREET
ALEXANDRIA, VA 22311
01CY ATTN J.M. AEIN
01CY ATTN ERNEST BAUER
01CY ATTN HANS WOLFARD
01CY ATTN JOEL BENGSTON

INTL TELL & TELEGRAPH CORPORATION
500 WASHINGTON AVENUE
NUTLEY, NJ 07110
01CY ATTN TECHNICAL LIBRARY

JAYCOR
P.O. BOX 85154
11011 TORREYANA ROAD
SAN DIEGO, CA 92138
01CY ATTN N.T. GLADD
01CY ATTN J.L. SPERLING

JOHNS HOPKINS UNIVERSITY
APPLIED PHYSICS LABORATORY
JOHNS HOPKINS ROAD
LAUREL, MD 20810
01CY ATTN DOC LIBRARIAN
01CY ATTN THOMAS POTEMRA
01CY ATTN JOHN DASSOULAS

KAMAN SCIENCES CORPORATION
P.O. BOX 7463
COLORADO SPRINGS, CO 80933
01CY ATTN T. MEAGHER

KAMAN TEMPO-CENTER FOR ADVANCED
STUDIES
816 STATE STREET
(P.O. DRAWER QQ)
SANTA BARBARA, CA 93102
01CY ATTN DASIAC
01CY ATTN WARREN S. KNAPP
01CY ATTN WILLIAM MCNAMARA
01CY ATTN B. GAMBILL

LINKABIT CORPORATION
10453 ROSELLE
SAN DIEGO, CA 92121
01CY ATTN IRWIN JACOBS

LOCKHEED MISSILES & SPACE CO., INC
P.O. BOX 504
SUNNYVALE, CA 94088
01CY ATTN DEPT 60-12
01CY ATTN D.R. CHURCHILL

LOCKHEED MISSILES & SPACE CO., INC
3251 HANOVER STREET
PALO ALTO, CA 94304
01CY ATTN MARTIN WALT/
DEPT 52-12
01CY ATTN W.L. IMHOF/
DEPT. 52-12
01CY ATTN RICHARD G. JOHNSON/
DEPT. 52-12
01CY ATTN J.B. CLADIS/
DEPT. 52-12

MARTIN MARIETTA CORPORATION
ORLANDO DIVISION
P.O. BOX 5837
ORLANDO, FL 32805
01CY ATTN R. HEFFNER

MCDONNELL DOUGLAS CORPORATION
5301 BOLSA AVENUE
HUNTINGTON BEACH, CA 02647
01CY ATTN N. HARRIS
01CY ATTN J. MOULE
01CY ATTN GEORGE MROZ
01CY ATTN W. OLSON
01CY ATTN R.W. HALPRIN
01CY ATTN TECHNICAL LIBRARY SERVICES

MISSION RESEARCH CORPORATION
735 STATE STREET
SANTA BARBARA, CA 03101
01CY ATTN P. FISCHER
01CY ATTN W.F. CREVIER
01CY ATTN STEVEN L. GUTSCHE
01CY ATTN R. BOGUSCH
01CY ATTN R. HENDRICK
01CY ATTN RALPH KILB
01CY ATTN DAVE SOWLE
01CY ATTN F. FAJEN
01CY ATTN M. SCHEIBE
01CY ATTN CONRAD L. LONGMIRE
01CY ATTN B. WHITE
01CY ATTN R. STAGAT
01CY ATTN D. KNEPP
01CY ATTN C. RINO

MISSION RESEARCH CORPORATION
1720 RANDOLPH ROAD, S.E.
ALBUQUERQUE, NM 87106
01CY ATTN R. STELLINGWERF
01CY ATTN M. ALME
01CY ATTN L. WRIGHT

MITRE CORPORATION
WESTGATE RESEARCH PARK
1820 DOLLY MADISON BLVD
MCLEAN, VA 22101
01CY ATTN W. HALL
01CY ATTN W. FOSTER

PACIFIC-SIERRA RESEARCH CORP
12340 SANTA MONICA BLVD
LOS ANGELES, CA 90025
01CY ATTN E.C. FIELD, JR

PENNSYLVANIA STATE UNIVERSITY
IONOSPHERE RESEARCH LAB
318 ELECTRICAL ENGINEERING EAST
UNIVERSITY PARK, PA 16802
UNIVERSITY PARK, PA 16802
01 CY ATTN IONOSPHERIC RESEARCH LAB

PHOTOMETRICS, INC.
4 ARROW DRIVE
WOBURN, MA 01801
01CY ATTN IRVING L. KOFSKY

PHYSICAL DYNAMICS, INC.
P.O. BOX 10367
OAKLAND, CA 04610
01CY ATTN A. THOMSON

R & D ASSOCIATES
P.O. BOX 9695
MARINA DEL REY, CA 90291
01CY ATTN FORREST GILMORE
01CY ATTN W.B. WRIGHT, JR
01CY ATTN W.J. KARZAS
01CY ATTN H. ORY
01CY ATTN C. MACDONALD
01CY ATTN BRIAN LAMB
01CY ATTN MORGAN GROVER

RAYTHEON CORPORATION
528 BOSTON POST ROAD
SUDBURY, MA 01776
01CY ATTN BARBARA ADAMS

RIVERSIDE RESEARCH INSTITUTE
330 WEST 42ND STREET
NEW YORK, NY 10036
01CY ATTN VINCE TRAPANI

SCIENCE APPLICATIONS INTERNATIONAL CORPORATION
10260 CAMPUS POINT DRIVE
SAN DIEGO, CA 92121-1522
01CY ATTN L.M. LINSON
01CY ATTN D.A. HAMLIN
01CY ATTN E. FRIEMAN
01CY ATTN E.A. STRAKER
01CY ATTN C.A. SMITH

SCIENCE APPLICATIONS INTERNATIONAL CORPORATION
1710 GOODRIDGE DRIVE
MCLEAN, VA 22102
01CY ATTN J. COCKAYNE
01CY ATTN E. HYMAN

SRI INTERNATIONAL
333 RAVENSWOOD AVENUE
MENLO PARK, CA 94025
01CY ATTN J. CASPER
01CY ATTN DONALD NEILSON
01CY ATTN ALAN BURNS
01CY ATTN G. SMITH
01CY ATTN R. TSUNODA
01CY ATTN D.A. JOHNSON
01CY ATTN W.G. CHESNUT
01CY ATTN C.L. RINO
01CY ATTN WALTER JAYE
01CY ATTN J. VICKREY
01CY ATTN R.L. LEADABRAND
01CY ATTN G. CARPENTER
01CY ATTN G. PRICE
01CY ATTN R. LIVINGSTON
01CY ATTN V. GONZALES
01CY ATTN D. MCDANIEL

TECHNOLOGY INTERNATIONAL CORP
75 WIGGINS AVENUE
BEDFORD, MA 01730
01CY ATTN W.P. BOQUIST

TRW DEFENSE & SPACE SYS GROUP
ONE SPACE PARK
REDONDO BEACH, CA 90278
01CY ATTN R.K. PLEBUCH
01CY ATTN S. ALTSCHULER
01CY ATTN D. DEE
01CY ATTN D. STOCKWELL/
SNTF/1575

VISIDYNE
SOUTH BEDFORD STREET
BURLINGTON, MA 01803
01CY ATTN W. REIDY
01CY ATTN J. CARPENTER
01CY ATTN C. HUMPHREY

UNIVERSITY OF PITTSBURGH
PITTSBURGH, PA 15213
01CY ATTN N. ZABUSKY